Received: 14 March 2018 | Revised: 4 August 2018 | Accepted: 5 October 2018

DOI: 10.1002/nme.5968

RESEARCH ARTICLE

WILEY

A mesh objective method for modeling crack propagation using the smeared crack approach

D. J. Burnett[1] | H. L. Schreyer[2]

[1]Sandia National Laboratories, Albuquerque, New Mexico

[2]Department of Mechanical Engineering, University of New Mexico, Albuquerque, New Mexico

Correspondence
D. J. Burnett, Sandia National Laboratories, P.O. Box 5800, Albuquerque, NM 87185.
Email: dburnet@sandia.gov

Summary

This paper presents a mesh objective method for modeling crack propagation in brittle materials using a conventional finite element formulation. The primary shortcoming of the smeared crack approach is its pathological sensitivity to the mesh orientation, which is manifested by shear locking and stress field misalignment around the crack tip. Such undesirable characteristics preclude the ability to model arbitrary crack propagation at an angle through the mesh. Several techniques are developed to address these shortcomings. First, to preclude shear locking, a modified failure constitutive model is developed, which projects out the spurious stress increments as the crack opens. If a crack exists in an element, a crack tracking algorithm is used to identify the neighboring elements most likely to show crack continuation. This algorithm also identifies a crossover element when a crack passes through adjacent sides of an element. Then, the characteristic element length used in the constitutive equation is changed with the objective of providing the correct failure energy per unit crack length, a procedure called crossover scaling. The examples provided demonstrate that the developed methods work collectively to provide a simple and efficient method for modeling failure in brittle materials without mesh bias.

KEYWORDS

crack tracking algorithm, crossover scaling, decohesion, mesh objective, smeared crack approach

1 | INTRODUCTION

The literature is replete with methods to predict crack propagation in a variety of materials from ductile metals to brittle concrete undergoing controlled quasi-static deformation to highly dynamic blast or penetration loading. The ultimate goal is to develop a robust numerical method that predicts the primary features observed in experimental data while at the same time providing results that are insensitive to the numerical discretization.

One of the first methods to represent a crack within a finite element was that of Rashid.[1] This approach became known as the smeared crack approach (SCA) and became popular due to its simplicity and implementation convenience. In SCA, the crack is represented continuously in an element where the stress and/or stiffness components are modified to represent the forces acting on an oriented crack surface. The crack orientation can be arbitrary and mesh topology need not change. The underlying conventional finite element formulation remains intact and the crack opening displacements are cast over the standard nodal degrees of freedom. However, the pathological sensitivity to the orientation of the mesh was the primary reason why SCA was abandoned over other methods such as the discrete approach originated by Ngo and Scordelis,[2]

the extended finite element method introduced by Belytschko and Black,[3] the phase-field approach from the works of Miehe et al[4] and Borden et al,[5] and nonlocal approaches such as in the works of Bažant and Lin[6] and Silling.[7]

Mesh size dependence in localization problems has been notably addressed by Hillerborg et al[8] for discrete cracks and Bažant and colleagues[9,10] for smeared cracks. In both cases, mesh size dependence is overcome by including the fracture energy and element size into the failure constitutive model. This essentially limits the dissipation of fracture energy to a fixed width equal to the element size. For the smeared crack case, this approach became known as the crack band theory.[10] Although the crack band theory was monumental in alleviating mesh size dependence for SCA, the approach did not address mesh orientation dependence. We note that a recent paper by Kurumatani et al,[11] which addresses mesh size dependence, presents an isotropic damage approach to modeling crack propagation in concrete structures.

A significant effort was made in the 1990s to resolve the issues with SCA such as those by Rots,[12,13] de Borst and Nauta,[14] Jirásek and Zimmerman,[15] and, more recently, by Cervera and Chiumenti[16,17] with limited success. A recent effort[18] using a mixed finite element formulation has shown that improved mesh objectivity is obtained if both strain and displacements are computed as unknowns at the nodes. This type of formulation requires twice as many unknowns as a standard finite element formulation and there are other stability issues to deal with related to the Babuška-Brezzi condition that complicate the implementation as well as reduce computational efficiency.

Methods that introduce a discontinuity within a finite element to enrich its degrees of freedom encompass embedded discontinuities.[19-23] The development of such methods was intended to help solve some of the issues associated with modeling strain localization and failure problems using finite elements. Embedded discontinuities expand the degrees of freedom of an element such that a discontinuity is represented within a single band inside the element. An enrichment of the standard element basis functions is made for either strain or displacement. Linder and Armero[22] used embedded discontinuities that provide additional modes of deformation for a crack opening to model failure in concrete. For example, a crack is allowed to open linearly across an element, whereas the standard approach is to assume a constant crack opening. These methods also require additional integration points along the discontinuity line.

We believe that the primary shortcoming of SCA is that the method introduces spurious strain components when the crack opening is incremented. Spurious components of strain cause spurious components of stress which, in turn, contributes to stress locking and incorrect predictions of the direction of crack propagation. In addition, the details of crack placement within an element are important; especially when a crack passes through adjacent sides of a rectangular element.

The objective of this paper is to provide the details that substantiate these claims and to provide modifications that rectify the problems. These changes are incorporated in a numerical algorithm. In Section 2, we attempt to provide a clear description of objectives and scope. In the next section, we show explicitly the source of the spurious strains for both Mode-I and Mode-II crack development. Then, in Section 4, we summarize the failure model, together with the smeared-crack implementation that includes a characteristic element length that provides the correct failure energy for an element, and the minimum element size that must be used to prevent stress reversal within an element. Section 5 provides the details of how a crack is tracked through the mesh and the adjustment that must be made when a crack crosses adjacent edges of an element. Next, the details of how spurious stresses are eliminated and the effect on element nodal forces are described in Section 6. With restriction to Mode-I failure, numerical solutions are shown in Section 6 to indicate that convergence is displayed with mesh refinement and experimental features are replicated. A summary is given in Section 7. The key result is that crack propagation is predicted using conventional element technology where the direction of the crack does not depend on mesh orientation or size. This is what we call a mesh objective method.

2 | AIMS AND SCOPE

In this paper, we interpret the standard SCA model as one of using the smeared crack method for numerically implementing a discrete constitutive equation with no further modifications. The method is computationally efficient, but it has proven to be inaccurate when a crack is not parallel to sides of an element and therefore cannot be considered a robust general approach. This work represents an initial study to identify the source of the problem and to propose a method to correct the issue. Here, we focus on individual cracks and neglect more complicated crack behavior such as crack branching, coalescence, and tortuosity. These are topics that can be addressed in subsequent studies.

One approach that removes stress locking utilizes a "rotating" crack concept within an element, which we think is somewhat unrealistic in that, once a crack initiates, it physically does not rotate. What we are suggesting is that there is perhaps a simpler way of looking at the problem. One aspect is to maintain traction consistent with the crack constitutive

equation and to fix the orientation within each element. If the crack is physically curved, then we allow the orientation in an adjacent element to reflect the direction in which the crack has propagated. This feature requires that the crack be physically followed through the mesh.

We focus on modeling tensile failure of materials that exhibit brittle behavior under small lateral compression such as concrete where the cohesive characteristics of the material govern the crack formation and shape of the load deflection curves.

The discontinuous failure model used involves just the normal component of traction and the mode of failure is only in the normal direction. The proposed approach was to prevent any shearing motion between crack surfaces or, in what is the same thing, do not allow any component of the displacement discontinuity vector perpendicular to that indicated by the model.

For simplicity, we use a standard finite element formulation where nodal displacements are the unknowns and standard shape functions are used. The specific finite element implementation used in this paper is similar to that provided in the work of Hughes[24] with computation of the nodal force vector rather than the stiffness matrix.

3 | SPURIOUS STRAIN

Spurious stress components are the root cause of stress locking when introducing cracks within standard finite elements. This section will quickly demonstrate why these stress components arise. In short, they arise due to the resulting strain relationships that result from the finite element formulation. Consider the geometry and element notation shown in Figure 1A with the normal to a microcrack in the x-direction.

With the use of the conventional isoparametric mapping, it can be shown that the components of strain evaluated at the center of the element for the planar problem are

$$e_{xx} = \frac{1}{2A}\left[(y_2 - y_4)(u_1 - u_3) + (y_3 - y_1)(u_2 - u_4)\right] \tag{1}$$

$$e_{yy} = \frac{1}{2A}\left[(x_4 - x_2)(v_1 - v_3) + (x_1 - x_3)(v_2 - v_4)\right] \tag{2}$$

$$\begin{aligned} e_{xy} = {} & \frac{1}{4A}\left[(x_4 - x_2)(u_1 - u_3) + (x_1 - x_3)(u_2 - u_4)\right] \\ & + \frac{1}{4A}\left[(y_2 - y_4)(v_1 - v_3) + (y_3 - y_1)(v_2 - v_4)\right], \end{aligned} \tag{3}$$

where x_i and y_i are the nodal coordinates, u_i and v_i are the nodal displacements in the x- and y-directions, respectively, and A is the element area.

Consider the Mode-I case and assume that a Mode-I crack forms in the center of the element with a crack opening displacement of $[[u_n]] = 2\delta$ as shown in Figure 1A. The crack normal defined by $\mathbf{n}$ is in the $\mathbf{e}_1$ direction as indicated by the local element crack $\{\mathbf{n}, \mathbf{t}\}$ basis in Figure 1A. The SCA formalism is applied and the crack opening displacement is represented via a displacement of nodes 1 through 4 such that the element expands by 2δ. The expanded element due

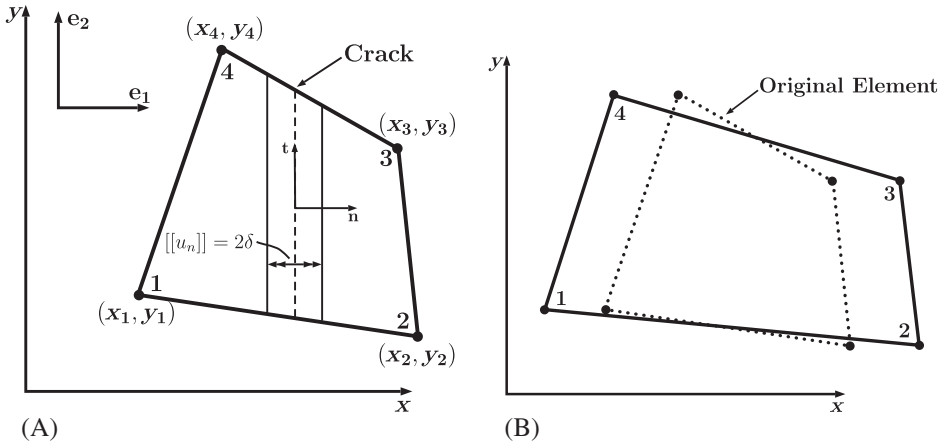

FIGURE 1 Mode-I Crack in four-node quadrilateral element. A, Initiated crack; B, Cracked element

to the crack opening is shown in Figure 1B where the original element geometry is represented by a dotted line. Because the crack opening is exclusively in the $\mathbf{e}_1$ direction, the nodal displacements in the $\mathbf{e}_2$ direction are equal to zero, or $v_1 = v_2 = v_3 = v_4 = 0$. One form for the nodal displacements in the normal direction that is consistent with geometry of a uniform crack is $u_1 = u_4 = -\delta$, and $u_2 = u_3 = +\delta$. The substitution of these displacement components in Equations 1 through 3 yields strains in the element due to the crack denoted e_{xx}^{cr}, e_{yy}^{cr}, and e_{xy}^{cr} as follows:

$$e_{xx}^{cr} = \frac{\delta}{A}(y_4 - y_2 + y_3 - y_1) \tag{4}$$

$$e_{yy}^{cr} = 0 \tag{5}$$

$$e_{xy}^{cr} = \frac{\delta}{2A}(x_1 - x_4 + x_2 - x_3). \tag{6}$$

The result shown in Equation 6 is the spurious shear strain contribution due to the crack opening. This parasitic shear strain increases linearly with the crack opening displacement. The spurious shear strain becomes zero if $\delta = 0$ or

$$x_1 - x_4 + x_2 - x_3 = 0. \tag{7}$$

Equation 7 is a geometric constraint on the element. One particular element geometry that satisfies Equation 7 is the case where the edges of the element are aligned with the crack surface or $x_1 = x_4$ and $x_2 = x_3$. Because the crack orientation is not known prior to mesh generation, it is not possible to prevent the possibility of spurious shear for the general case.

An alternative form for applying nodal displacements to simulate a crack within a finite element to preclude spurious strains is presented in an earlier work.[25]

A similar analysis can be completed for Mode-II cracks. Now, a crack is introduced in shear with crack opening displacement $[[u_t]] = 2\delta$ in the $\mathbf{t}$ direction. Applying nodal displacements of $u_1 = u_2 = u_3 = u_4 = 0$ and $v_1 = v_4 = -\delta$ and $v_2 = v_3 = +\delta$ results in the following strain components:

$$e_{xx}^{cr} = 0 \tag{8}$$

$$e_{yy}^{cr} = \frac{\delta}{A}(x_2 - x_3 + x_1 - x_4) \tag{9}$$

$$e_{xy}^{cr} = \frac{\delta}{2A}(y_4 - y_2 + y_3 - y_1). \tag{10}$$

Notice now that, from Equation 9, a spurious normal strain e_{yy} is obtained. Similar to the Mode-I crack, if the element edges are parallel to the crack or $x_1 = x_4$ and $x_2 = x_3$, the spurious normal strain vanishes.

The use of a constitutive model will result in spurious stress components due to the presence of these spurious strain components.

4 | FAILURE MODEL

4.1 | Overview of a decohesion model

The discrete failure model proposed in this paper is a decohesion model that uses a decohesion function F to provide the correct failure orientation defined by the crack normal vector $\mathbf{n}$, failure stress, fracture energy G, and evolution of failure as the crack opens. This type of model is a cohesive crack model where the relationship between the traction $\boldsymbol{\tau}$ and crack opening displacement $[[\mathbf{u}]]$ is specified. The failure orientation is computed by finding the crack normal vector that maximizes the decohesion function. The failure surface is defined by the locus of points where the decohesion function is equal to zero in some stress space typically of principal stress. Finally, the evolution of failure is incorporated into the failure model using a softening function f_s that defines how the traction changes with a change in crack opening displacement. The softening function can be either linear or nonlinear.

A decohesion model is therefore a very powerful and direct approach to modeling cracks in a material as the crack characteristics are explicit. These features are not inherent in nonlocal continuum models where the mode of failure is not derived from the failure model itself but is deduced from the path of failed elements based on the numerical solution. A decohesion model is formulated as an analogy to rate independent plasticity where the decohesion function is analogous to the yield function, the crack opening displacement vector is analogous to the plastic strain tensor, the traction is analogous to the stress tensor, and the softening function is analogous to the hardening function.

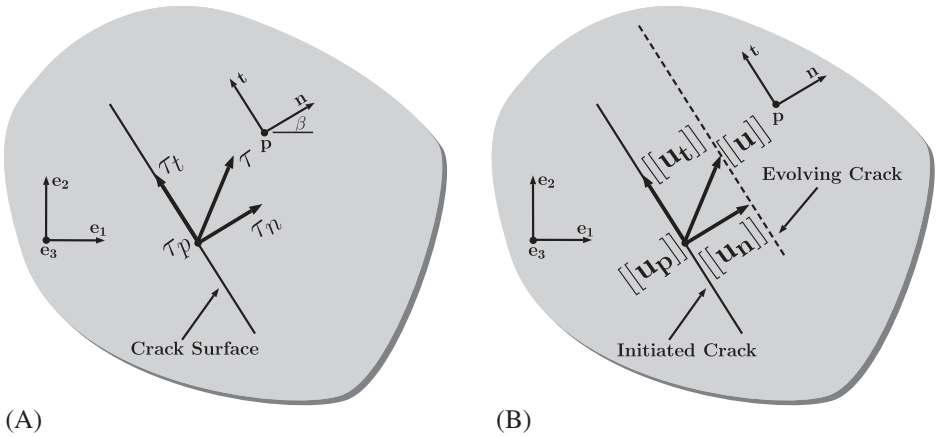

FIGURE 2 Failure model crack representation. A, Traction; B, Crack opening displacement

4.2 | Generalized constitutive equations

The key idea behind the constitutive equations is to update the stress in the cracked element without introducing spurious stress components. Certain components of the stress are projected out to preclude pollution of the numerical solution due to spurious shear stress. It is important to note that the preclusion of spurious stress is not the full story behind enabling a standard finite element formulation to model cracks with mesh objectivity. This will hopefully be clear as we progress through this paper. Another important aspect is that the crack orientation is assumed fixed after crack initiation and does not rotate as is assumed in the rotating crack model. This allows the actual physical crack path to be predicted more accurately. A microcrack is defined to be a crack for which there is still a residual strength, while a macrocrack denotes the situation where two free surfaces exist.

The model begins with the assumption that microcracking is initiated along an oriented plane of failure defined by a unit normal vector $\mathbf{n}$. A local orthonormal basis is constructed by adding two unit orthogonal vectors $\mathbf{t}$ and $\mathbf{p}$ defined such that $\mathbf{p} = \mathbf{n} \times \mathbf{t}$, where $\mathbf{p}$ is out of the plane shown in Figure 2. The traction is represented by the vector $\boldsymbol{\tau} = \tau_n \mathbf{n} + \tau_t \mathbf{t} + \tau_p \mathbf{p}$ as shown in Figure 2A. The corresponding crack opening displacement vector $[[\mathbf{u}]]$ is shown in Figure 2B where $[[\mathbf{u}]] = [[u_n]]\mathbf{n} + [[u_t]]\mathbf{t} + [[u_p]]\mathbf{p}$. The crack then evolves as the crack opening displacement $[[\mathbf{u}]]$ increases while the traction $\boldsymbol{\tau}$ decreases. The traction is obtained from the stress as follows:

$$\boldsymbol{\tau} = \boldsymbol{\sigma} \cdot \mathbf{n}. \tag{11}$$

Implicit with the formulation is that components of vectors and tensors must be transformed between a global basis and the local basis. A discrete failure model defines the relationship between the traction $\boldsymbol{\tau}$ and the crack opening displacement $[[\mathbf{u}]]$. Mathematically, the failure model provides the function $\boldsymbol{\tau} = \boldsymbol{\tau}([[\mathbf{u}]])$ through the use of evolution equations.

The possibility of initial failure, or continuing failure, for a particular orientation identified by the unit normal $\mathbf{n}$ at a material point, is indicated with the use of a failure decohesive function $F_n(\tau_n, f_n)$ constructed such that $F_n < 0$ implies failure evolution is not occurring, $F_n = 0$ indicates that failure evolution is possible, and $F_n > 0$ is not allowed. The softening function f_n provides the current state of failure as a function of $\bar{u}_n$, which is a scalar measure of the development of failure or effective decohesion. We choose $\bar{u}_n$ to be of the dimensionless form

$$\bar{u}_n = \frac{[[u_n]]}{u_0}, \tag{12}$$

where u_0 is a reference displacement.

Prior to the formation of a microcrack, all orientations for $\mathbf{n}$ must be considered and the worst case is used to identify a specific choice for $\mathbf{n}$. To this end, we define a general decohesive function as follows:

$$F = \max_{\forall \mathbf{n}} F_n. \tag{13}$$

The orientation of the unit normal to the crack surface and the local orthonormal basis are obtained by finding the crack normal $\mathbf{n}$ that maximizes the value of the decohesion function under the assumption that the normal lies in the plane of maximum and minimum stress. The details of this procedure is described in the work of Xu et al.[26]

During a loading scenario for a given problem, all material points must be checked continuously for the possibility of failure initiation. With numerical procedures, these points are finite in number and explicitly defined. If $F < 0$, then the failure condition is not satisfied and the continuum constitutive equation holds for that point. A crack is initiated once $F > 0$. In a numerical procedure for this material point, storage is allocated for the components of $\mathbf{n}$, the components of the displacement continuity, and the effective decohesion $\bar{u}_n$. There may be more than one material failure surface at any one material point.

For subsequent times in the loading scenario, if the failure function for one of the orientations satisfies $F > 0$, then that microcrack or macrocrack is allowed until the condition that $F_n = 0$ is satisfied. Then, other orientations are considered to see if an additional failure surface with a different orientation is created for the same material point. If an additional surface is created, then storage must be allocated for the corresponding variables, just as they were for the first crack. Finally, other material points are investigated to see if new microcracks are initiated.

The evolution equations related to decohesion are chosen to be the following:

$$[[\dot{\mathbf{u}}]] = \dot{\omega}\tau_{nf}\frac{\partial F_n}{\partial \boldsymbol{\tau}} \tag{14}$$

$$\dot{\bar{u}} = \frac{\dot{\omega}}{u_0} \tag{15}$$

$$\dot{F}_n = 0, \tag{16}$$

where ω is a monotonically increasing parameter introduced for convenience to parameterize the equations and u_0 is the magnitude of normal crack opening at which the traction first becomes zero. The last equation is the consistency condition.

The decohesion function used for this study is the Rankine criterion

$$F_n = \frac{\tau_n}{\tau_{nf}} - f_n, \tag{17}$$

so that during failure, the condition $F_n = 0$ is equivalent to

$$\tau_n = \tau_{nf}\, f_n. \tag{18}$$

It is assumed that f_n is constructed to be a monotonically decreasing function with $f_n(0) = 1$. Two forms for the softening function have been used. The first is that of linear softening

$$f_n = \begin{cases} 1 - \bar{u}_n, & 0 \le \bar{u}_n \le 1 \\ 0, & \bar{u}_n > 1, \end{cases} \tag{19}$$

ie, u_0 is chosen to be the opening at which the traction first becomes zero. The form of Equation 19 provides the following physical interpretation. If $f_n = 1$ ($\bar{u}_n = 0$), failure has not initiated. If $1 > f_n > 0$ ($0 < \bar{u}_n < 1$), a microcrack has developed. Finally, if $f_n = 0$ ($\bar{u}_n \ge 0$), the microcrack has evolved to a macrocrack or equivalently to a crack with two new free surfaces generated. If the fracture energy is defined to be

$$G_f = \int_0^{u_0} \tau_n d\,[[u_n]]\,, \tag{20}$$

then

$$u_0 = \frac{2G_f}{\tau_{nf}}. \tag{21}$$

For exponential softening, we return to the same dimensionless form for the effective decohesion and assume the softening function to be

$$f_n = \exp(-\alpha\bar{u}_n), \quad 0 \le \bar{u}_n < \infty, \tag{22}$$

which indicates that, with a large crack opening, traction carrying capacity is never lost but becomes negligibly small. The fracture energy is

$$G_f = \int_0^{\infty} \tau_{nf}\, f_n d\,[[u_n]] = \tau_{nf}\, u_0 \int_0^{\infty} \exp(-\alpha\bar{u}_n) d\bar{u}_n = \frac{\tau_{nf}\, u_0}{\alpha}. \tag{23}$$

Then, the set of Equations 14 through 16 becomes

$$[[\dot{u}_n]] = \dot{\omega}, [[\dot{u}_t]] = 0, [[\dot{u}_p]] = 0 \tag{24}$$

$$\dot{\bar{u}} = \frac{[[\dot{u}_n]]}{u_0} \tag{25}$$

$$0 = \frac{\dot{\tau}_n}{\tau_{nf}} + \kappa \dot{\bar{u}}_n, \tag{26}$$

in which $\kappa = 1$ for linear softening and $\kappa = \alpha \exp(-\alpha \bar{u}_n)$ for nonlinear softening. We note that $[[\dot{u}_n]] \geq 0$ so that $\dot{\tau}_n \leq 0$.

For a given decohesion rate, crack strain rates are defined that are assumed to be constant over the element. The components of the crack strain rate for an element are computed in the $\{n, t\}$ basis following the strong discontinuity kinematic formulation of Oliver[27]

$$\dot{e}^{cr}_{nn} = \frac{[[\dot{u}_n]]}{h_c}, \dot{e}^{cr}_{tt} = 0, \dot{e}^{cr}_{nt} = 0, \tag{27}$$

where h_c is the characteristic element size. The characteristic element size is computed from the size of the element h using the orientation of the crack β as follows:

$$h_c = \begin{cases} \frac{h}{\cos\beta}, & -\frac{\pi}{4} \leq \beta \leq \frac{\pi}{4} \\ \frac{h}{\sin\beta}, & \frac{\pi}{4} \leq \beta \leq \frac{3\pi}{4} \end{cases}. \tag{28}$$

The rate forms of the isotropic elasticity equations are

$$\dot{\sigma}_{nn} = E_1 \left(\dot{e}_{nn} - \dot{e}^{cr}_{nn}\right) + E_2 \dot{e}_{tt} \tag{29}$$

$$\dot{\sigma}_{tt} = E_2 \left(\dot{e}_{nn} - \dot{e}^{cr}_{nn}\right) + E_1 \dot{e}_{tt} \tag{30}$$

$$\dot{\sigma}_{nt} = 2G\dot{e}_{nt}, \tag{31}$$

where E_1 and E_2 assume the following forms for plane stress and plane strain:

$$E_1 = \begin{cases} \frac{Y}{1-\nu^2}, & \text{plane stress} \\ \frac{Y(1-\nu)}{(1+\nu)(1-2\nu)}, & \text{plain strain} \end{cases} \tag{32}$$

$$E_2 = \begin{cases} \frac{\nu Y}{1-\nu^2}, & \text{plane stress} \\ \frac{\nu Y(1-\nu)}{(1+\nu)(1-2\nu)}, & \text{plain strain,} \end{cases} \tag{33}$$

where Y is Young's modulus, ν is Poisson's ratio, and G is the shear modulus.

The consistency equation is provided in Equation 26. Because $\tau_n = \sigma_{nn}$ and $e^{cr}_{nn} = [[u_n]]/h_c$, it follows that, with the use of Equation 25,

$$\dot{\sigma}_{nn} = -\tau_{nf} \frac{\kappa h_c}{u_0} \dot{e}^{cr}_{nn}. \tag{34}$$

Then, Equation 29 yields

$$E_1 \left(\dot{e}_{nn} - \dot{e}^{cr}_{nn}\right) + E_2 \dot{e}_{tt} = -\tau_{nf} \frac{\kappa h_c}{u_0} \dot{e}^{cr}_{nn}. \tag{35}$$

The rate of crack strain becomes

$$\dot{e}^{cr}_{nn} = \frac{1}{\Psi} \left(E_1 \dot{e}_{nn} + E_2 \dot{e}_{tt}\right) \tag{36}$$

in which

$$\Psi = E_1(1-\gamma), \quad \gamma \equiv \frac{\kappa h_c}{u_0} \frac{\tau_{nf}}{E_1}. \tag{37}$$

In terms of the tangent tensor components, the rate forms of the elasticity equations are

$$\dot{\sigma}_{nn} = T_{nn} \dot{e}_{nn} + T_{nt} \dot{e}_{tt} \tag{38}$$

$$\dot{\sigma}_{tt} = T_{tn} \dot{e}_{nn} + T_{tt} \dot{e}_{tt} \tag{39}$$

$$\dot{\sigma}_{nt} = 2G\dot{e}_{nt}, \tag{40}$$

where

$$T_{nn} = E_1\left(1 - \frac{E_1}{\Psi}\right) = -E_1\frac{\gamma}{1-\gamma} \tag{41}$$

$$T_{tt} = E_1 - \frac{E_1 E_2}{\Psi} = \frac{1}{E_1(1-\gamma)}\left[E_1^2(1-\gamma) - E_2^2\right] \tag{42}$$

$$T_{nt} = E_2\left(1 - \frac{E_1}{\Psi}\right) = -E_2\frac{\gamma}{1-\gamma}. \tag{43}$$

We note that $T_{tn} = T_{nt}$.

For all paths such that $\dot{e}_{nn}^{cr} > 0$, we require $\dot{\sigma}_{nn} < 0$. Suppose we consider a set of radial paths defined by $\dot{e}_{tt} = \eta\dot{e}_{nn}$ for arbitrary but constant values of η. Suppose we assume $\Psi > 0$ and $\dot{e}_{nn} > 0$. The condition $\dot{e}_{nn}^{cr} > 0$ yields

$$E_1 + \eta E_2 > 0. \tag{44}$$

Then,

$$\dot{\sigma}_{nn} = T_{nn}\dot{e}_{nn} + T_{nt}\dot{e}_{tt} = \dot{e}_{nn}(T_{nn} + \eta T_{nt}). \tag{45}$$

To prevent a stress reversal, we require

$$T_{nn} + \eta T_{nt} < 0. \tag{46}$$

However,

$$T_{nn} + \eta T_{nt} = -\frac{\gamma}{1-\gamma}(E_1 + \eta E_2). \tag{47}$$

Therefore, Equations 44 and 37 yield

$$\frac{\gamma}{1-\gamma} > 0 \quad \text{or} \quad 0 < \gamma < 1. \tag{48}$$

The restriction of Equations 48 and 37 imposes a maximum element size that can be used for numerical simulations. The characteristic element size must then satisfy

$$h_c \leq \frac{E_1 u_0}{\kappa\tau_{nf}}. \tag{49}$$

With use of Equations 21, 23, and 49, the element size restriction in terms of the fracture energy G_f is

$$h_c \leq \begin{cases} \frac{2E_1 G_f}{\tau_{nf}^2}, & \text{linear softening} \\ \frac{E_1 G_f}{\tau_{nf}^2}, & \text{nonlinear softening.} \end{cases} \tag{50}$$

5 | KEY COMPONENTS FOR MESH OBJECTIVITY

We have observed that precluding spurious shear is only one of many components that must be introduced for both mesh size and orientation objectivity when a standard finite element formulation is used with the SCA to model crack propagation. This section provides an overview of each of these components.

5.1 | Numerical setup

To illustrate the potential merits of the proposed approach, we have limited the scope of the investigation. First, the numerical procedure used to obtain solutions to static problems is that of dynamic relaxation, which is interpreted here to mean a viscous damper is attached to each node. Such an approach is elementary and provides a solution with little overshoot, a feature that is important when crack initiation is very sensitive to the value of stress. The second restriction involves the choice of element type to illustrate the insensitivity of mesh orientation to direction of crack propagation. Oriented meshes are constructed by starting with a rectangular mesh configuration and rotating two sides of the elements in a graded fashion as indicated in Figure 3 with the maximum angle of rotation located at the center of the domain.

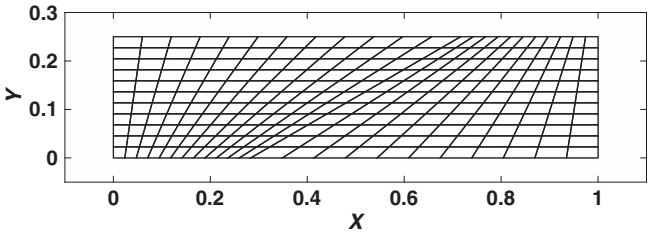

FIGURE 3 Mesh design used in numerical studies

5.2 | Precluding spurious shear stress

For Mode-I cracking, we note that, at crack initiation, the shear stress is zero. As the crack opening evolves, this may become nonzero due to two causes: (i) the stress path may change so that the shear is naturally nonzero and (ii) the spurious result that is a consequence of element geometry as discussed previously. When the microcrack evolves to become a macrocrack, the traction, and specifically the shear component, on the crack surface is zero unless the loading path changes to force the crack closed, a situation not being considered here. Therefore, there is a small loading segment in which the shear may legitimately be nonzero. Here, we look at the simplification of setting the shear stress identically to zero for the loading segment, an approach that corrects the potential development of the spurious shear and is a simplifying assumption for the shear when such a component may actually be nonzero due to the change in loading path.

It is possible to separate the portion of the shear due to an increment in crack opening and remove just this portion of the stress. This additional feature has not been included because the intent of this paper is to indicate that the basic idea is of merit to explore in more detail. The full formulation would consider the appropriate adjustment to preclude only the spurious part of the traction vector that should be made for mixed-mode failure.

The failure model introduced in Section 4.2 in Equations 38 through 43 is inherently susceptible to spurious shear stress. The reason for this is because upon incrementing a crack strain within a standard quadrilateral element (or triangle), a spurious shear strain will arise as demonstrated in Section 3. Observing Equation 40, the rate of shear stress $\dot{\sigma}_{nt}$ is a function of the rate of shear strain $\dot{e}_{nt}$ and the shear modulus G. For Mode-I failure, the crack opening displacement is strictly in the direction normal to the crack. As a result, during a crack increment, there should be no change in shear stress due to the crack. We assume the pretense of brittle failure where, upon crack initiation, the material cannot support shear stress. As a result, we assume that $\dot{\sigma}_{nt} = 0$. The constitutive equations become

$$\dot{\sigma}_{nn} = T_{nn}\dot{e}_{nn} + T_{nt}\dot{e}_{tt} \tag{51}$$

$$\dot{\sigma}_{tt} = T_{tn}\dot{e}_{nn} + T_{tt}\dot{e}_{tt} \tag{52}$$

$$\dot{\sigma}_{nt} = 0. \tag{53}$$

5.3 | Crack tracking algorithm

A separate approach is necessary to provide the correct crack path because the predicted crack tends to naturally follow the element edges even when there is no spurious stress in the numerical solution. This happens because the stress field around the crack tip is misaligned with respect to the crack orientation determined from the failure model. This leads to an inability in predicting curved crack trajectories in which the crack must traverse the mesh at an angle.

Finite element approaches that have been successfully used to provide the correct crack path are of two primary categories: (i) nonlocal damage, stress, or strain measure and (ii) a crack tracking algorithm. Some examples of the first for modeling concrete include the works of Bažant and Lin,[6] Jirasek and Zimmermann,[28] and Geers et al.[29] Although, using a nonlocal measure can preclude some mesh dependence on the crack path, it requires additional computational expense. This is because the nonlocal measure is typically computed by taking an average of some variable, usually strain, over a neighborhood of points centered around the integration point.

A more direct approach is to explicitly determine the crack path and allow failure to occur exclusively on this predicted path. This approach is applied in crack tracking algorithms. Crack tracking algorithms do not necessarily preclude stress misalignment in a direct sense. Rather, the elements that would normally initiate failure during stress misalignment are not allowed to fail. Only elements that lie on the predicted crack path are allowed to fail and this restriction essentially realigns the stress field around the crack. However, crack tracking algorithms are susceptible to error because they can

only be as good as the predicted crack orientation. For failure models that assume that the crack orientation is related to the principal stress basis, spurious shear can alter the predicted crack orientation and therefore lead to incorrect crack paths.

The crack tracking algorithm used in this study is a local tracking method that uses the crack orientation computed from the failure model to form continuous line segments that define the crack path. We consider this to be an elementary tracking approach and make no claims of its applicability to more complex crack problems that might involve branching and sharply curved cracks. However, these types of problems are beyond the scope of the current study, and the tracking method used performs its function as intended. Further examples of crack tracking approaches can be found in the work of Cervera and Chiumenti[30] and, more recently, in the works of Slobbe et al[31] and Saloustros et al.[32]

Even though the crack tracking algorithm provided in the Appendix may not be new or unique, the details of the specific tracking algorithm used in this paper are included for the sake of completeness and can be further studied in an earlier work.[25] The uniqueness of the crack tracking algorithm in this paper stems from applying it to detect crack crossovers, which is required to maintain the correct characteristic crack dimension. If a crack intersects the opposite sides of an element and not adjacent sides, the actual position of the crack plays no part in the expression for the smeared crack strain. However, if a physical crack crosses adjacent sides of an element in what we call a crossover feature, then the two elements exhibit crack strain. Unless an adjustment is made, the dissipated energy per unit crack length is different than the value exhibited for a crack in a single element. Furthermore, if this feature is not taken into account in the numerical algorithm as loading progresses, crack strains will appear in a broadening band of elements.

5.4 | Reduced integration

For the four-node quadrilateral element, full integration requires four quadrature points. This complicates the modeling of crack propagation because each element would then possess four cracks each with a different crack orientation and crack opening displacement. As many others have done, we use one-point quadrature.

There are two cases to deal with: (i) the continuous or uncracked element and (ii) the cracked element. For the continuous case, a standard hourglass control procedure can be used. We employed the hourglass control method of Flanagan and Belytschko[33] for the continuous case. For the second case, when a crack is initiated in an element, we set the hourglass forces for that element to zero. As a result, hourglass control is used exclusively in uncracked elements.

5.5 | Crack crossover scaling

The characteristic crack dimension h_c plays an important role in crack propagation problems. When crack crossovers occur, it is important to adjust h_c such that the crack dimension is equal to the sum of the element dimensions h that compose the crossover. We denote adjusting h_c for crossover cracks as *crossover scaling* or COS. For example, the crossover crack composed of elements D and E in Figure A1 possesses a characteristic crack dimension of $h_c = h^D + h^E$, where h^D and h^E are the element sizes for elements D and E, respectively. The crack tracking algorithm is used to identify when crossover cracks occur and thus when to activate COS.

Let us examine more closely the implications of adjusting h_c. The key crack tangent modulus component from Section 4.2 is restated here as

$$T_{nn} = -E_1 \frac{\gamma}{1-\gamma}, \tag{54}$$

where

$$\gamma = \frac{h_c \tau_{nf}}{u_0 C_{11}}. \tag{55}$$

For softening and no snapback where snapback is defined to be the case where $T_{nn} > 0$, we require $\gamma < 1$, which leads to the following inequality obtained in Equation 49:

$$h_c \leq \frac{E_1 u_0}{\kappa \tau_{nf}}.$$

If γ is increased, subject to the constraint on h_c, then the magnitude of the softening slope is also increased. For the crossover case, the characteristic crack length is the sum of the element dimensions that compose the crossover. An increase in h_c automatically adjusts the increase in softening slope and the dissipated fracture energy for the two elements

is equivalent to the fracture energy dissipated in one element. As a result, the energy dissipated in the crossover becomes consistent to the energy dissipated in adjacent cracked elements that consist of only one element. As a result, the stress in cracked and nearby uncracked elements remains consistent and stress field distortion is eliminated as will be demonstrated in Section 6.

6 | RESULTS

6.1 | Mode-I model problem and mesh configurations

We choose a model problem that allows a focused examination of the effects of both mesh size and orientation as shown in Figure 4. A slender bar is chosen such that the shear stress near the ends of the bar are minimal for a nonzero Poisson's ratio. The left end of the bar is held fixed in the x- and y-directions while, at the right end of the bar, the displacement is prescribed with $u(1, y, t) = v_c t$ with $v_c = 0.0001$. The bar is allowed to laterally contract at $x = 1$. The top and bottom surfaces are traction free.

A crack is initiated in the center of the bar by reducing the tensile strength of the center element. The crack is then allowed to propagate across the bar in a manner predicted by the crack tracking algorithm. The material properties are shown in Figure 4 where $\nu = 0.2$, $Y = 1$, $\rho = 1$, $\tau_{nf} = 0.011$, and the tensile strength of the element that initiates failure $\tau^f_{nf} = 0.01$. Viscous nodal damping is used for dynamic relaxation with a damping coefficient $c = 4$ chosen to smooth out the load deflection curves. The following meshes are considered with maximum slant angle θ: (1) $\theta = 0$, (2) $\theta = 30°$, (3) $\theta = 60°$, where the maximum slant angle occurs in the center of the bar as shown in Figure 5. For each rotation, three

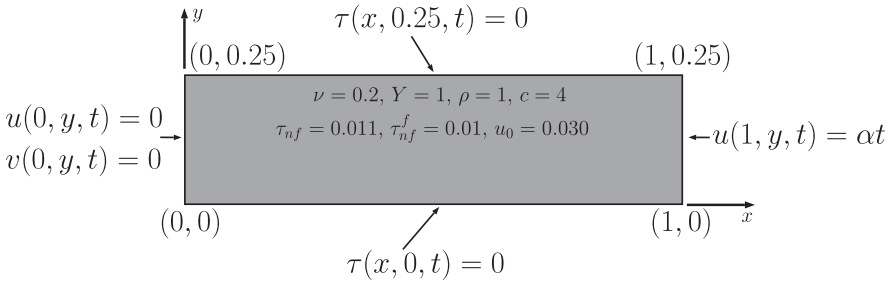

FIGURE 4 Slender bar pulled in tension

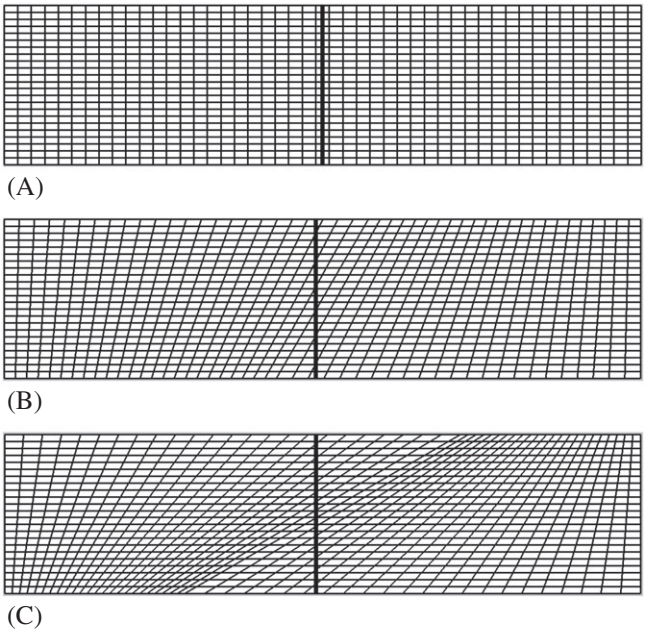

FIGURE 5 Meshes used with various orientations and expected crack paths. A, $\theta = 0°$; B, $\theta = 30°$; C, $\theta = 60°$

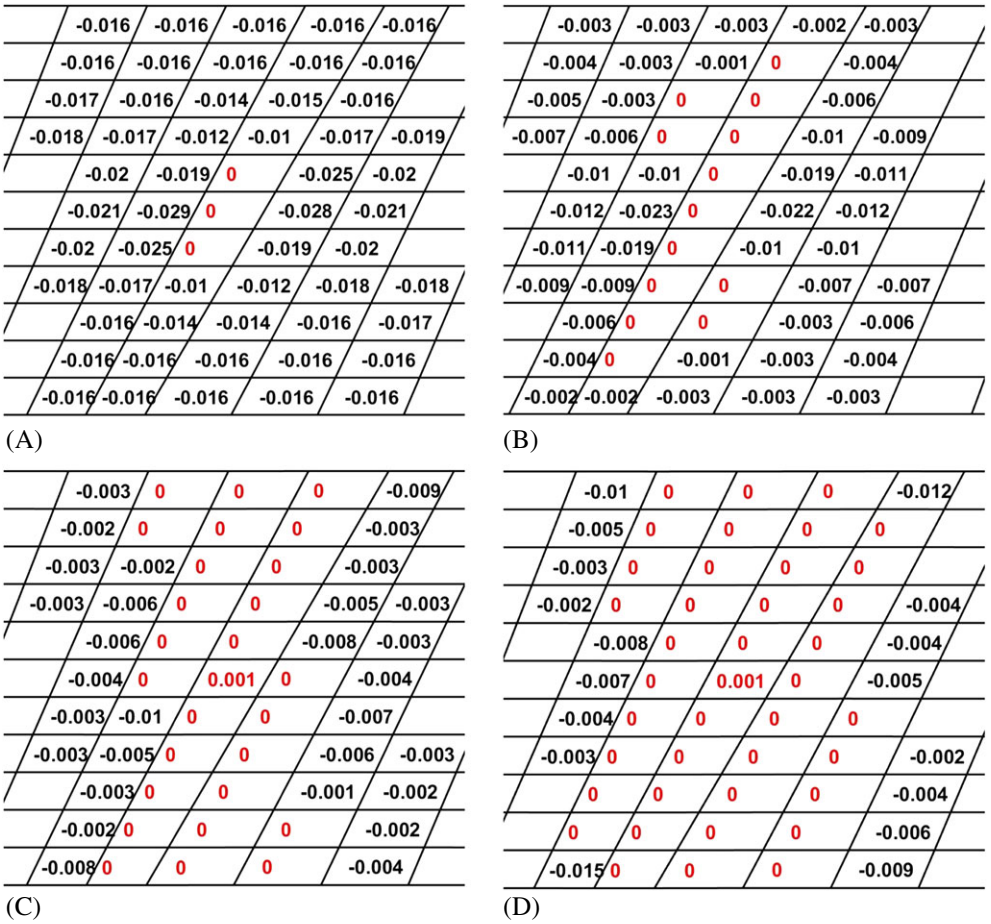

FIGURE 6 Crack elements for standard smeared crack approach [Colour figure can be viewed at wileyonlinelibrary.com]

different meshes each containing $N_x \times N_y$ elements in the x- and y-directions, respectively, are as follows: (i) 11×5, (ii) 23×11, and (iii) 47×23. For comparison purposes, the results obtained using a standard decohesion failure model are also shown where they are noted. We consider the set of equations as a standard decohesion model provided in Section 4.2, but without modification of the shear stress rate and COS. The performance metrics are the predicted crack paths and load-deflection curves.

6.2 | Illustration of proposed features in comparison with standard SCA

We investigate the various aspects of our proposed approach by looking at the evolution of crack growth from the center, which has been assigned a slightly smaller value of failure stress. The first result is shown in Figure 6 for the standard smeared crack algorithm by which we mean the application of the set of equations in Section 4.2 to any element that exhibits a positive value of the failure function without modification to stresses, crack tracking, and COS. Elements displaying cracks are shown as red values of the failure function, which should be a small positive value close to zero, depending on the tolerance value used in the algorithm. Figure 6A shows the expected initiation, but then, Figures 6B and 6C show the spreading out of cracked elements that extends to the domain shown in Figure 6D and vividly demonstrates the potential problem with the standard SCA approach.

Next, in Figure 7, we show the effect of crack evolution when spurious shear stresses are removed. Now, the orientation of the crack within each element is correct but the crack path itself is obviously incorrect. However, now, without spurious shear stress polluting the solution, the crack is a single element in width.

Finally, Figure 8 shows the evolution of crack development when crack tracking and COS is added to the previous step of removing spurious shear. The final crack is a vertical line through the cracked elements shown in Figure 8D and shows two crossover elements.

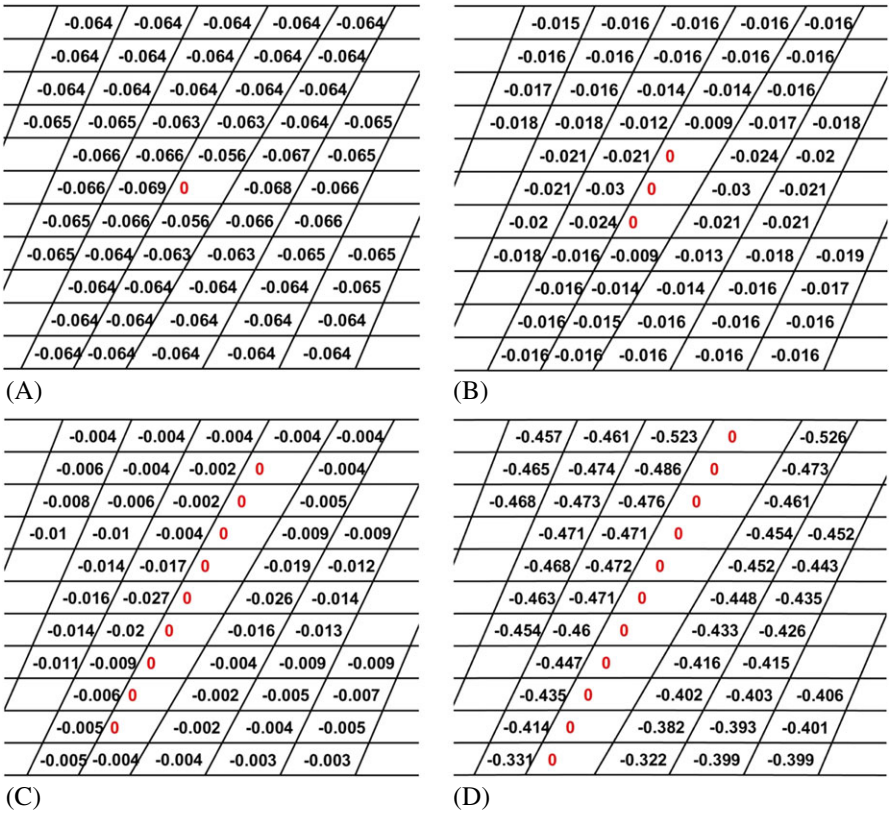

FIGURE 7 Crack elements without spurious shear [Colour figure can be viewed at wileyonlinelibrary.com]

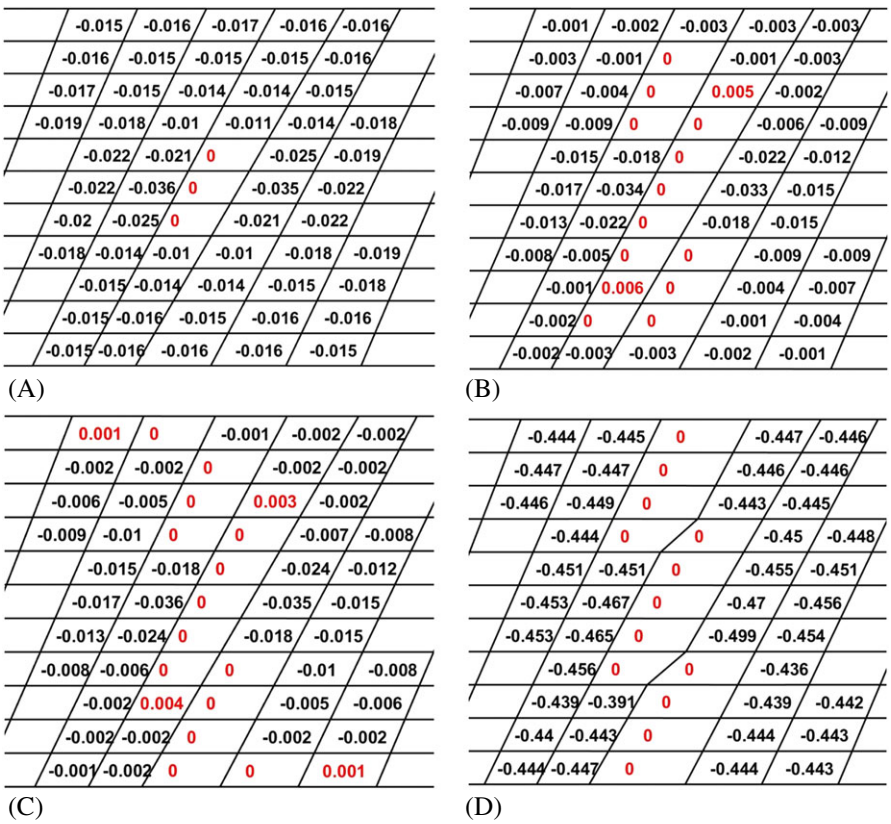

FIGURE 8 Crack elements without spurious shear, with crack tracking, and with crossover scaling [Colour figure can be viewed at wileyonlinelibrary.com]

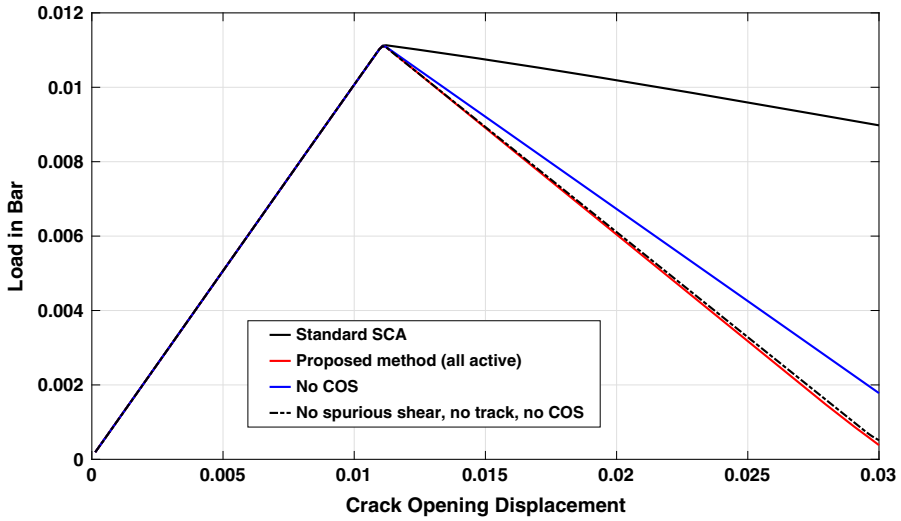

FIGURE 9 Effects of various model components. COS, crossover scaling; SCA, smeared crack approach [Colour figure can be viewed at wileyonlinelibrary.com]

The load displacement curves associated with these various cases are shown in Figure 9. The stress locking associated with the conventional SCA results in a load-displacement curve much too high in the post-peak regime. The red line is associated with the application of all three aspects consisting of removing spurious stresses, crack tracking, and COS. This solution agrees with the analytical solution based on the assumption that the crack opens uniformly across the bar. It is interesting to note that, when only spurious shear removal is used, there is very little difference in the load-deflection curve from the analytical solution. However, as noted previously, the predicted crack pattern is clearly erroneous. When COS is not used, the blue line is obtained, and this shows that not enough energy dissipation is being achieved.

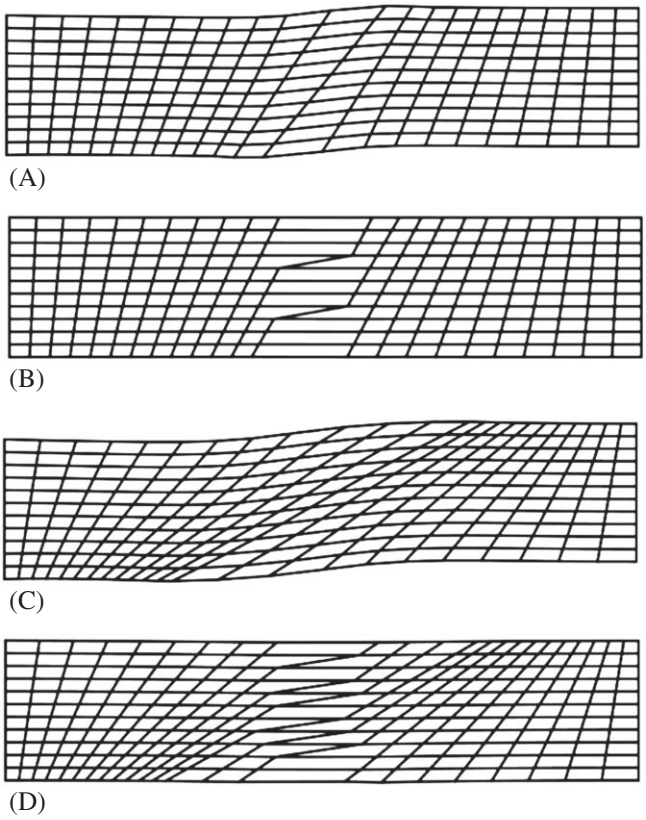

FIGURE 10 Final mesh state at full crack opening. A, Standard smeared crack approach (SCA) model: $\theta = 30°$; B, Proposed model: $\theta = 30°$; C, Standard SCA model: $\theta = 60°$; D, Proposed model: $\theta = 60°$

An additional comparison is made in Figure 10 with standard SCA by looking at mesh distortion for both 30° and 60° mesh orientations. For the present problem, the crack should open horizontally. Figure 10 compares the final state of the mesh for a displacement scaling factor of 5 for the proposed and standard SCA models for $\theta = 30$ and $\theta = 60°$. Notice that, in Figure 10A, the standard SCA model provides a distorted crack opening. For $\theta = 60°$, the standard SCA model cannot introduce a crack opening due to the extent of shear locking as shown in Figure 10B. In contrast, the proposed model provides essentially the same crack opening regardless of mesh orientation as shown in Figures 10C and 10D.

6.3 | Mesh size and orientation study

To investigate the effects of mesh orientation and size, for each mesh size, the load-deflection curves are plotted for all mesh slant angles as shown in Figure 11. The results provided in Figure 11 show that there is essentially no sensitivity to the orientation of the mesh. The differences in the predicted peak load are attributed to the mesh size and not the mesh orientation because, as the mesh is refined, these differences become smaller. The predicted crack paths for all cases defined in Figure 11 are the expected straight lines shown in Figure 5.

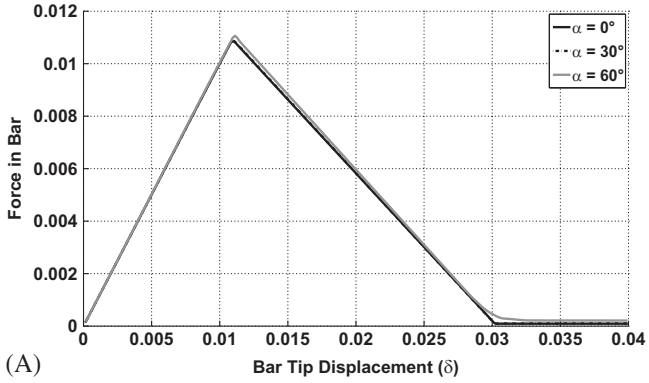

(A)

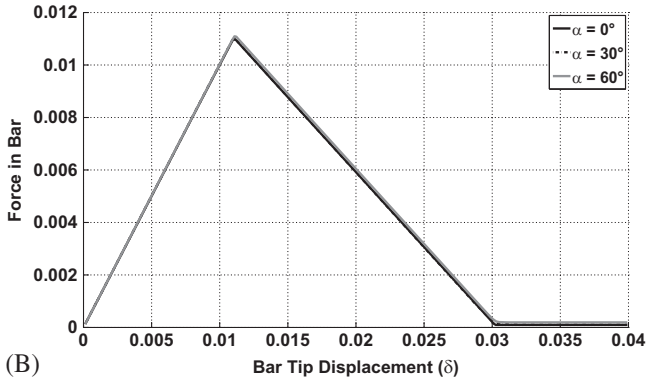

(B)

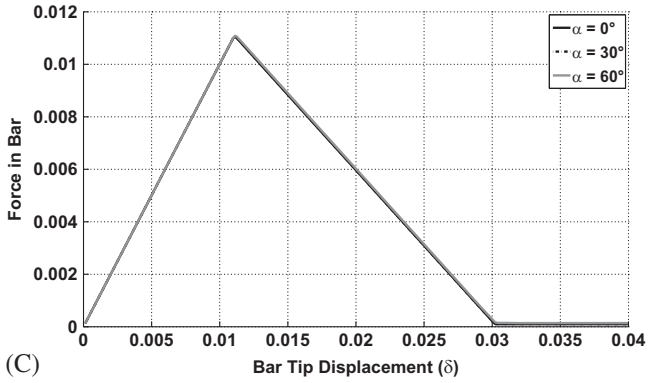

(C)

FIGURE 11 Effect of mesh orientation on load deflection curve. A, 11 × 5 mesh; B, 23 × 11 mesh; C, 47 × 23 mesh

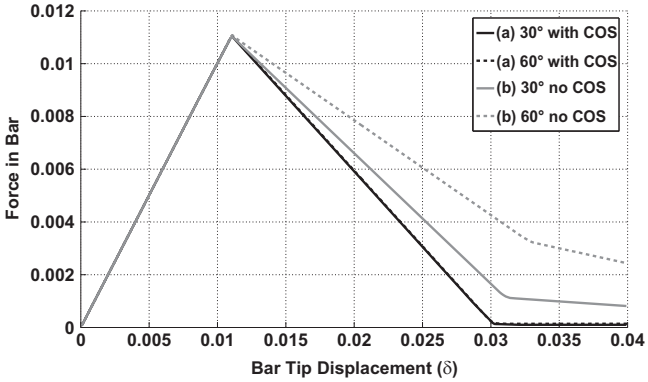

FIGURE 12 Effects of characteristic crack dimension h_c. COS, crossover scaling

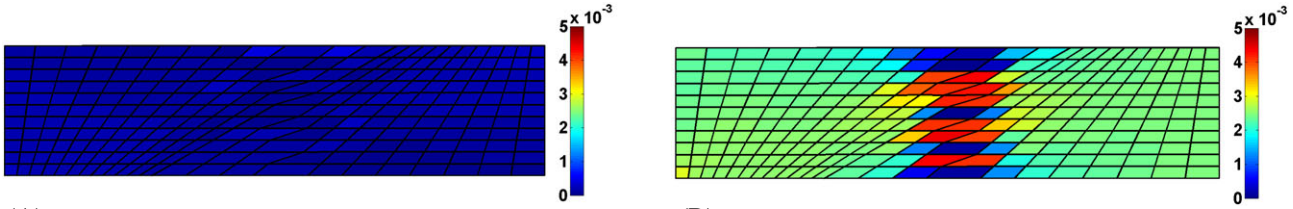

FIGURE 13 Spurious normal stress without crossover scaling (COS). A, With COS; B, Without COS [Colour figure can be viewed at wileyonlinelibrary.com]

6.4 | Importance of crossover scaling

We will consider the 23 × 11 mesh from Section 6.1 with orientations of $\theta = 30°$ and $\theta = 60°$. Two cases will be considered for each orientation: (a) with COS for crack crossovers such that h_c is the total width of the crossover and (b) without COS.

The load deflection curves are shown in Figure 12. Notice that, when the dimension of the crack is adjusted properly for crossovers in case (a), the 30° and 60° meshes obtain essentially the same load-deflection curve indicating that the stress in the bar is decaying to zero. However, when the crack dimension is not adjusted for crossover cracks, then there is mesh orientation bias. The mesh orientation bias becomes increasingly worse as the mesh orientation increases for case (b). This suggests that, without COS, mesh objectivity cannot be achieved.

A stiffening response is obtained for case (b) indicating that normal stress is accumulating in the bar as the crack opens. Figure 13 compares the normal stress σ_{xx} in the bar for $\delta = 0.04$. Notice that, with COS turned on, as shown in Figure 13A, the normal stress in the bar is uniform and close to zero. However, with COS turned off, as shown in Figure 13B, large normal stresses are centered around crack crossovers. This suggests that there is an inconsistency in the rate of unloading between crossover elements and adjacent cracked elements. By increasing h_c for all elements within the crossover, this causes the crossover elements to unload at the same rate as adjacent elements, and as a result, there is no spurious normal stress accumulation. This was the final piece of the puzzle that provided complete mesh objectivity.

6.5 | Double-edge-notch direct tension

Now, we turn to real experiments where a crack initiates due to a stress concentration brought on by a geometric discontinuity. A detailed and thorough research effort to characterize brittle material failure of double-edge-notch (DEN) concrete specimens was conducted by Nooru-Mohamed[34] in the early 1990s. Here, we simulate experiments from the aforementioned work[34] that focus on 0.2 × 0.2 × 0.050 m concrete specimens possessing two 0.025 × 0.005 m notches as illustrated in Figure 14.

The first loading case examined in this section is of direct tension where the specimen is pulled axially in tension under displacement control. Platens that are glued to the top and bottom surfaces are used to apply the controlled displacement. The tensile force and the crack opening displacement are both monitored throughout the duration of the experiment. The displacement δ_c, shown in Figure 14, is defined as the crack opening displacement. Finite element simulations of

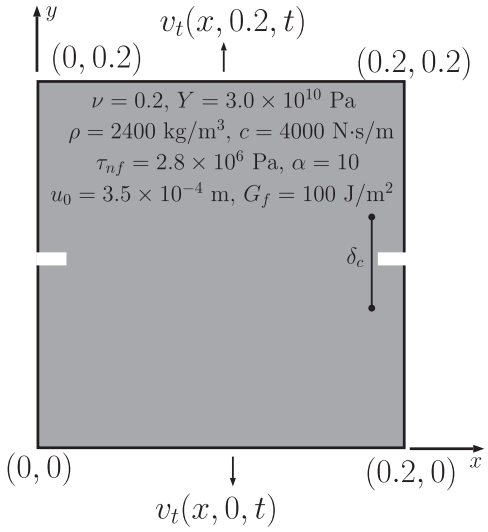

FIGURE 14 Double-edge-notch direct-tension problem setup

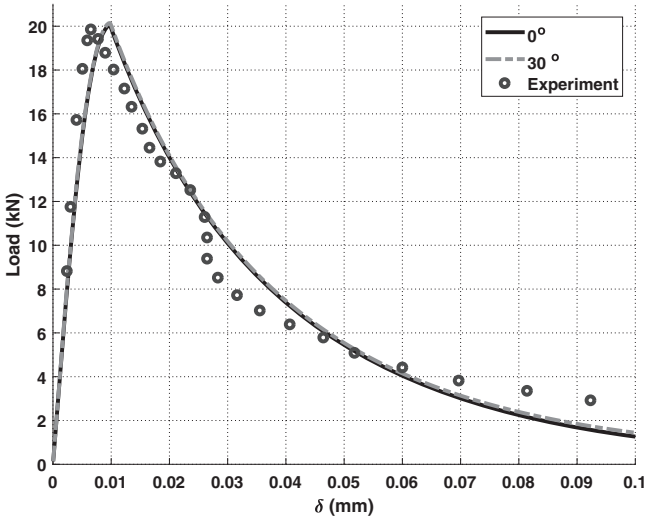

FIGURE 15 Load-deflection curve: double-edge-notch direct tension

the experiment were conducted by applying a uniform displacement over the bottom edge of $v(x, 0, t) = -v_c t$ and over the top edge of $v(x, 0.2, t) = v_c t$ with $v_c = 0.00025$ m/s. The horizontal displacement along the bottom and top edges was set to zero or $u(x, 0, t) = u(x, 0.2, t) = 0$. Traction-free boundary conditions were assumed on the left and right edges or $\boldsymbol{\tau}(0, y, t) = \boldsymbol{\tau}(0.2, y, t) = 0$.

The elastic material properties assumed were $\rho = 2400$ kg/m^3, $Y = 3.0 \times 10^{10}$ Pa, and $\nu = 0.2$. Viscous damping is applied assuming a damping coefficient of $c = 4000$ N · s/m. Nonlinear softening was used with $\tau_{nf} = 2.8 \times 10^6$ Pa, $\alpha = 10$, and $u_0 = 3.5 \times 10^{-4}$ m. Note that a fracture energy of $G_f = 100$ J/m^2 was used to compute u_0 using Equation 23.

Two 41 × 41 meshes with $\theta = 0$ and $\theta = 30°$ were used to discretize the concrete specimen. Each mesh consisted of 1671 quadrilateral elements and 1764 nodes. Note that the oriented mesh is shown later in Figure 16B. The crack tracking algorithm with COS was also used.

The resulting load-deflection curves are shown in Figure 15 with the experimental data. We first note that the load-deflection curves for the 0° and 30° meshes are nearly the same. This demonstrates that the proposed method is obtaining results that are not sensitive to the orientation of the mesh.

We next discuss the differences between the predicted load-deflection curve and the experimental data. First, the predicted load of the specimen during load up between $\delta = 0$ and $\delta = 0.01$ mm is smaller than what was measured in the experiment. Upon initial loading for $\delta < 0.002$ mm, the predicted load matches that of the experiment that would correspond to elastic material behavior. However, as the peak load is reached, the predicted curve becomes somewhat shifted in

δ as compared to the measured response. This may be attributed to a more localized region of failure initiation in the specimen during the experiment as compared to what was assumed in the simulation. In the simulation, failure initiates in a single element within the root of each notch, which is rather large. This element fails well before the peak load is reached and this plays an important role in the shape of the load-deflection curve prior to the peak load. If a greater portion of the material is assumed to initiate failure, this perhaps generates a softer response as compared to the experiments.

For this simulation, an exponential decay was used for the softening function so that a macrocrack is never achieved. Therefore, it is not surprising that the predicted load-deflection curve diverges from experimental data for large δ. A simple modification to the softening function that provides a nonzero contribution for large δ would offer more accurate

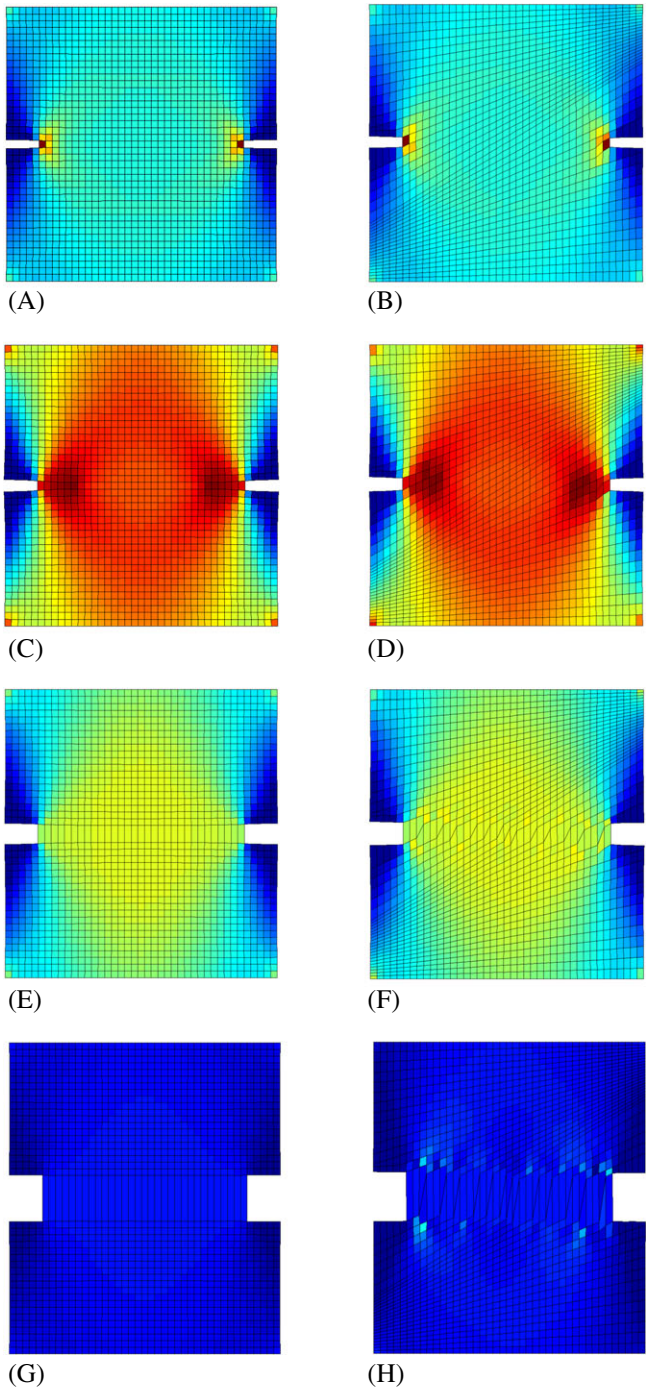

FIGURE 16 Normal stress contours from double-edge-notch direct-tension simulations (left column: regular mesh; right column: oriented mesh $\theta = 30°$). A, $\delta = 0.0031$ mm; B, $\delta = 0.0030$; C, $\delta = 0.0071$; D, $\delta = 0.0071$; E, $\delta = 0.024$; F, $\delta = 0.024$; G, $\delta = 0.074$; H, $\delta = 0.074$ [Colour figure can be viewed at wileyonlinelibrary.com]

results. However, the key point is that using a simple algorithm and relying on material properties alone, the key features observed in experimental data are predicted reasonably well without mesh orientation bias.

The normal stress contours are provided for both meshes for a few different simulation steps in Figure 16. The scale has been left off for clarity, but the minimum normal stress equal to zero is represented with a blue color and the maximum stress equal to $\tau_{nf} = 2.8 \times 10^6$ Pa is represented with red. The left column shows normal stress contours for $\theta = 0°$ and the right column shows normal stress contours for $\theta = 30°$. The results at the same simulation step are shown for comparison. Note that the displacements have been scaled by 400 to highlight the crack opening. The results show that the normal stress contours are very similar for the two meshes further demonstrating mesh objectivity. In addition, the displacement δ obtained from the two meshes are essentially the same as noted in the captions for Figure 16. For the 30° mesh, there are a few uncracked elements along the crack that have slightly higher normal stress than the bulk material. The locations of these *hotspots* are near crack crossovers. It is suspected that, even though COS dramatically reduces the effects associated with crack crossovers, the approach employed is not exact. As a result, there will be some elements that may contain slightly higher normal stresses. However, this only mildly affects the resulting load-deflection curve. Future research could improve the COS methods such that these hotspots are completely removed. It is noted that stress contours are typically not provided for crack propagation problems in the literature especially for different mesh orientations.

6.6 | DEN shear tension

In the previous section, the loading conditions were such that a crack propagated straight across the DEN specimen. In this section, we examine the algorithm's ability to predict curved crack trajectories by adding a shear loading stage. The experiments were conducted under load path 4 as described in the work of Nooru-Mohamed.[34] The DEN specimen geometry is identical to that of Section 6.5. The only difference is the boundary conditions imposed on the specimen.

The loading of the specimen consists of two loading stages. In the first stage, controlled lateral displacements u_s are applied uniformly to the top-left and bottom-right surfaces of the specimen as shown in Figure 17 such that the specimen is put into a state of lateral shear. The axial displacements are then controlled such that the net force acting on the specimen in the y-direction is zero. The lateral force is monitored while the lateral displacements are being applied. After the desired lateral force F_s is obtained, the second loading stage begins.

In the second loading stage, the lateral force F_s is held constant while the specimen is pulled in tension. The lateral displacements are adjusted such that the lateral force is held at F_s while the top and bottom surfaces are placed under displacement control. As the specimen cracks, the lateral displacements are appropriately adjusted to provide a constant lateral force.

This presents a challenging set of boundary conditions for the finite element simulations. Because the effective stiffness of the specimen is nonlinear due to the formation of cracks, an iterative method must be added to the main load increment loop that computes u_s such that a constant lateral force is maintained as the specimen cracks. A secant algorithm was chosen that is essentially Newton's method that approximates the derivative of the residual with respect to the lateral displacement. A residual is formed by taking the difference between the experimentally prescribed lateral force, F_s, and the calculated lateral force obtained by summing the normal stress-area products of all the elements that compose the lateral surfaces. The iterations continue until the residual is less than a specified tolerance.

The loading of the specimen goes as follows in the finite element simulations. Lateral displacements $u_s(0, y, t) = v_s t$ and $u_s(0.2, y, t) = -v_s t$ are prescribed with $v_s = 0.0002$ m/s for $0.105 \leq y \leq 0.2$ and $0 \leq y \leq 0.095$ m, respectively. At the

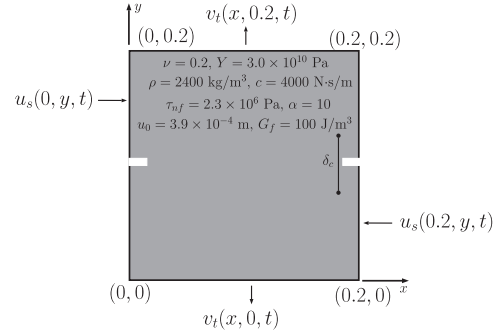

FIGURE 17 Double-edge-notch shear-tension problem setup

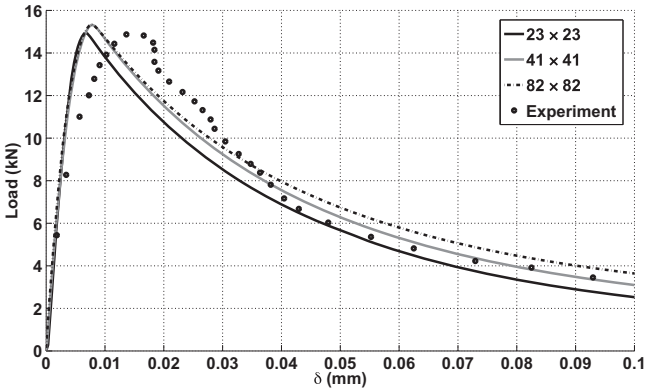

FIGURE 18 Load-deflection curve: shear tension ($F_s = 5$ kN)

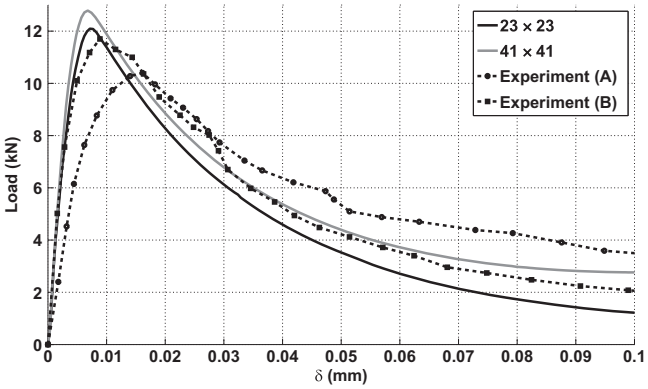

FIGURE 19 Load-deflection curve: shear tension ($F_s = 10$ kN)

same time, axial displacements $v_t(x, 0, t)$ and $v_t(x, 0.2, t)$ are proportionally prescribed such that the net axial force is close to zero. Because the stiffness of the material is nearly constant during the first loading stage, a proportionality constant that relates v_t to u_s is used to keep the axial force close to zero. Once the lateral force is greater than the set point F_s, then the axial displacements $v_t(x, 0, t)$ and $v_t(x, 0.2, t)$ are incremented starting from where they left off from the first loading stage. The secant algorithm iterations are then performed for all subsequent time steps that control the magnitude of $u_s(0, y, t)$ and $u_s(0.2, y, t)$ for every increment in the axial displacements v_t such that a constant lateral force is maintained. Note that it is assumed that $u_s(0, y, t) = -u_s(0.2, y, t)$.

The material properties used in the DEN direct-tension simulations in Section 6.5 were carried over with the exception of the tensile strength. In the work of Nooru-Mohamed,[34] it was observed that, in experiments that used four platens, the measured tensile strength was smaller than experiments that only used two platens. Note that the extra two platens are placed along the lateral edges for $0.105 \leq y \leq 0.2$ and $0 \leq y \leq 0.095$ m, respectively. In the DEN shear-tension experiments, four platens were used. As a result, the tensile strength was scaled based on direct-tension experiments obtained using four platens to $\tau_{nf} = 2.3 \times 10^6$ Pa with a corresponding $u_0 = 3.9 \times 10^{-4}$ m.

The material properties used here were $\rho = 2400$ kg/m^3, $Y = 3.0 \times 10^{10}$ Pa, and $\nu = 0.2$. Viscous damping was applied assuming a damping coefficient of $c = 4000$ N · s/m. Nonlinear softening was used with $\tau_{nf} = 2.3 \times 10^6$ Pa, $\alpha = 10$, and $u_0 = 3.9 \times 10^{-4}$ m.

Various meshes were chosen to investigate sensitivity to mesh size. Square meshes of 23×23, 41×41, and 82×82 were chosen. Two different lateral shear loads of 5 and 10 kN were studied. Note that, for the 23×23 mesh, the notch size was 0.026×0.009 m, which is larger than the actual notch size of 0.025×0.005 m.

The resulting load deflection curves for the $F_s = 5$ and 10 kN cases are shown in Figures 18 and 19, respectively. The experimental data are also provided. Note that, for the 10 kN case, there are two experimental data sets shown, which represent two separate experiments of similar concrete materials. Figure 18 shows that the predicted loading phase is stiffer than the experimental result. This is in contrast to the DEN direct-tension experiments in which the predicted load-up response was softer than what was measured. This might suggest that the material damage that occurs in the experiment during nucleation and propagation of microcracks is more diffuse than what is assumed in the simulation.

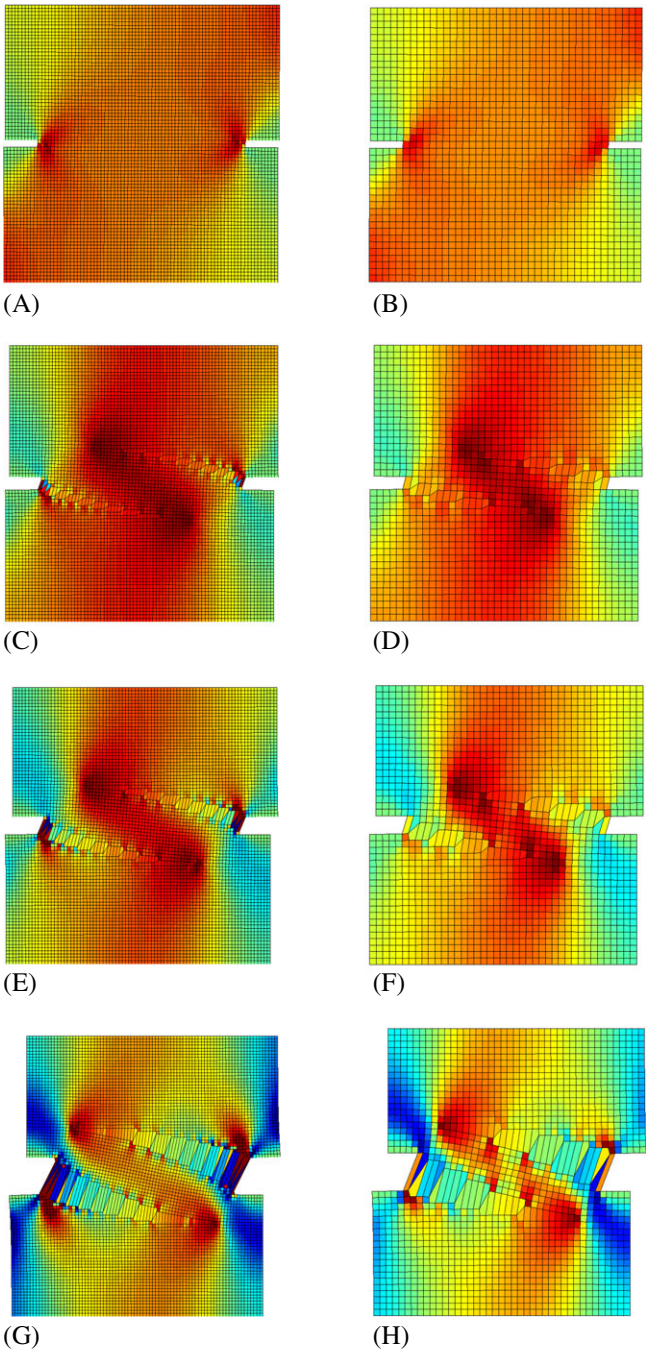

FIGURE 20 Normal stress contours (σ_{yy}) from double-edge-notch shear-tension simulations. A, $\delta = 0.0028$ mm; B, $\delta = 0.0029$; C, $\delta = 0.024$; D, $\delta = 0.024$; E, $\delta = 0.044$; F, $\delta = 0.044$; G, $\delta = 0.123$; H, $\delta = 0.123$ [Colour figure can be viewed at wileyonlinelibrary.com]

The simulation assumes that failure initiates only in two locations located near the notch root. As a result, the quantity of microcracks within the actual experiment could be much larger of which would create a softer loading response. It is emphasized that failure initiation occurs before the peak load is reached. Recall that the discrete failure model is an approximation to the complex nucleation of microcracks that do not necessarily occur on a single failure plane. Therefore, it is not too surprising that there is some error in the predicted load-up response of which includes this complex material failure process. The key point is that, even with an approximate failure model and a relatively coarse mesh, the features observed in the experiments can be predicted with relatively little mesh dependence.

The predicted stress contours suggest that, for the most part, the stress distribution within the concrete specimen is mesh objective. In Figures 20 and 21, the normal stresses for the 82×82 mesh are shown in the left column and the normal stresses for the 41×41 mesh are shown in the right column for a shear load of $F_s = 5$ kN. The minimum scale

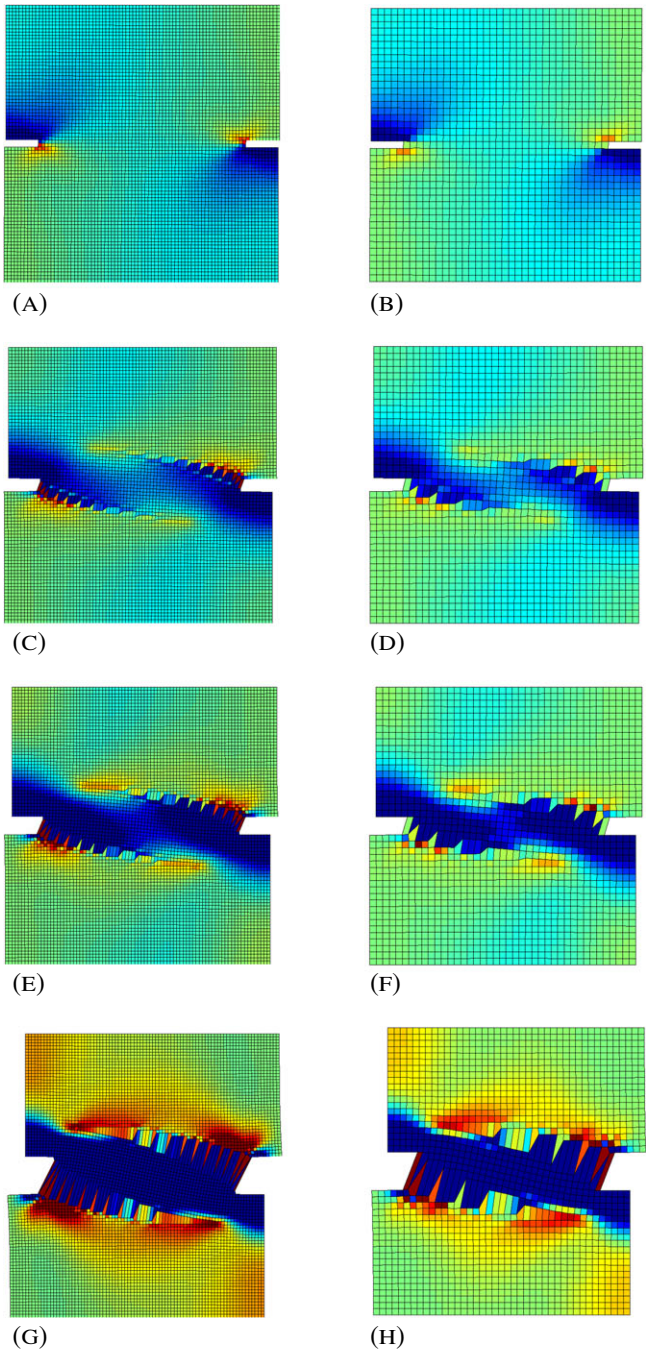

FIGURE 21 Normal stress contours (σ_{xx}) from double-edge-notch shear-tension simulations. A, $\delta = 0.0028$ mm; B, $\delta = 0.0029$; C, $\delta = 0.024$; D, $\delta = 0.024$; E, $\delta = 0.044$; F, $\delta = 0.044$; G, $\delta = 0.123$; H, $\delta = 0.123$ [Colour figure can be viewed at wileyonlinelibrary.com]

value was set to -2.3×10^6 Pa and is represented with blue colors. The maximum scale was set to 2.3×10^6 Pa and is represented with red colors. A state of zero stress is represented by green. The normal stress contours provided in Figure 20 highlight the propagation of the crack as shown in the localized region of high normal stress at the crack tip. Note that the displacements have been scaled by a factor of 200 to highlight the crack opening.

For the 82×82 mesh, there is a small region of large normal stress (σ_{yy}) near the notch. The coarser 41×41 mesh does not possess as strong of stress magnitudes within these areas. It is suspected that this feature is caused from not allowing the crack to propagate away from the notch toward the left and right sides of the specimen. The crack gets essentially pinned or stuck, and as a result, stress accumulates near the notch. We suspect that it is the higher stresses within this region that causes the load-deflection curve to shift upward as the mesh is refined. The fact that the stress distributions in the 41×41 and 82×82 meshes are similar further suggests that the shift in the load-deflection curve is a result of the

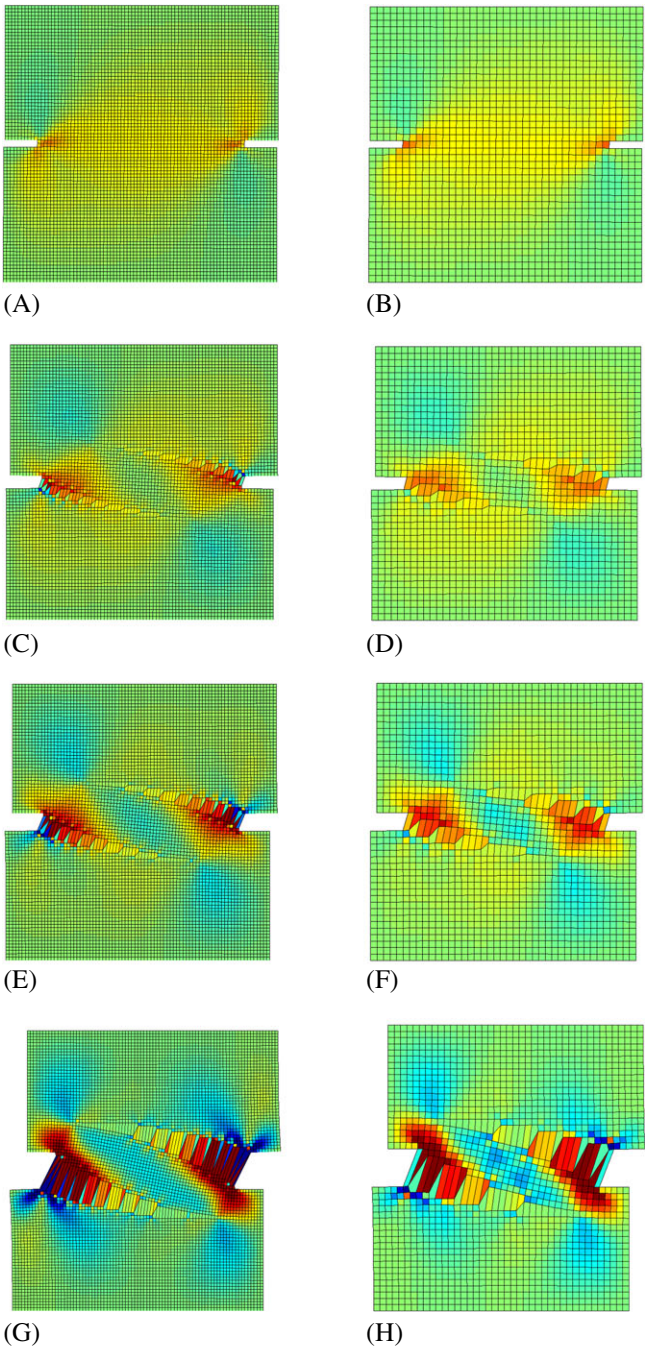

FIGURE 22 Shear stress contours (σ_{xy}) from double-edge-notch shear-tension simulations. A, $\delta = 0.0028$ mm; B, $\delta = 0.0029$; C, $\delta = 0.024$; D, $\delta = 0.024$; E, $\delta = 0.044$; F, $\delta = 0.044$; G, $\delta = 0.123$; H, $\delta = 0.123$ [Colour figure can be viewed at wileyonlinelibrary.com]

larger localized stresses in the notch area. These effects get worse as the lateral load increases. We do not believe that the shift in the load deflection curve is caused by mesh bias due to the crack propagation. Fixing this is a matter of fine-tuning the crack tracking algorithm to allow additional cracks to form around the notch.

Observing the normal stresses (σ_{xx}) in Figure 21 shows a transfer of stress into the center of the DEN specimen once the crack begins to propagate. This suggests that, once the microcrack forms, the center portion of the specimen goes into compression due to applied lateral compressive load. As the microcrack continues to propagate and open, the material that is adjacent to the crack goes into tension. If cracks were allowed to form in this region, then other microcracks would initiate and the stresses in these areas would decrease.

The shear stress (σ_{xy}) is plotted in Figure 22. Upon crack initiation at each notch, there is a large shear stress where the crack orientation is greatest. As the crack propagates, this shear stress increases in expanse. It is noted that the shear

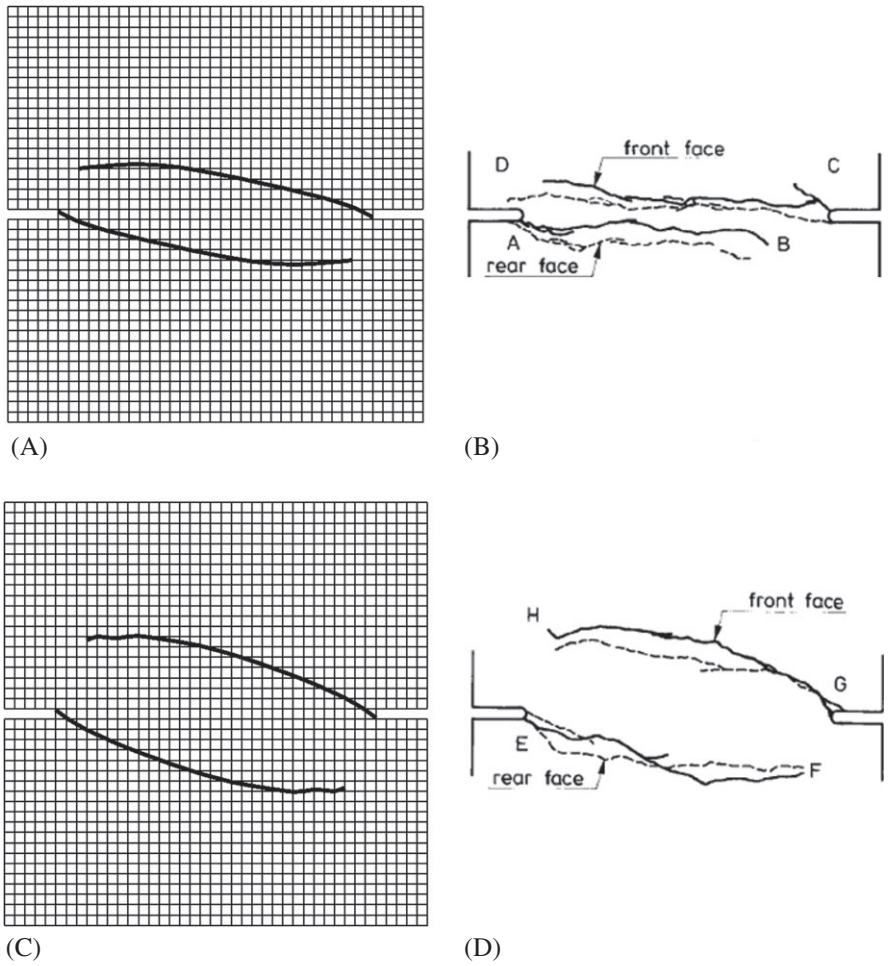

FIGURE 23 Crack patterns for double-edge-notch shear-tension problem. A, Predicted: 5 kN; B, Experiment: 5 kN[34]; C, Predicted: 10 kN; D, Experiment: 10 kN[34]

stress where the crack normal is nearly parallel to the y-axis or vertical is close to zero. Large shear stresses accumulate in areas where the crack normal contains the largest orientation. This would be consistent to what is allowed in the failure model. Once the crack orientation $\mathbf{n}$ is parallel to the y-axis, then we would expect that the shear in the global basis σ_{xy} to be close to zero. This is what we observe in Figure 22. Note that the large shear stresses near the notch could also be an artifact of the crack getting pinned as discussed earlier.

Finally, Figure 23 shows the predicted crack paths for the 41×41 mesh for both lateral shear loads. Notice that the crack predicted for the 10 kN lateral force contains more curvature than that predicted for the 5 kN lateral force, which is consistent with the experiments. The predicted crack curvature for the 5 kN case is slightly too large compared to experiment. However, this is primarily due to the crack branching that occurs in the experiment. The initial crack curvature near the notch in the experiment is consistent to that predicted from the simulation.

7 | SUMMARY

In this paper, the following methods were proposed: (1) Mode-I decohesion failure model that precludes spurious shear stress along the crack surface but keeps the crack orientation fixed as the crack evolves, (2) a crack tracking algorithm that provides the correct crack path, and (3) a COS method that provides the correct energy dissipation as a crack segment passes through adjacent sides of two elements. All three components are necessary in order to alleviate mesh orientation bias with respect to the crack path and the load-deflection curve.

A discrete failure model has the inherent properties that both a crack orientation and a mode of failure are predicted, and these features can be compared with those displayed by experimental data. Such features are not explicitly provided by

nonlocal continuum damage models but must be inferred from the path of failed elements based on a numerical solution. In addition, once a crack is initiated with the discrete model, the orientation remains fixed, an aspect that is considered physically realistic.

Because of its computational simplicity, the combination of a discrete failure model with the smeared crack numerical approach has been used in a large number of publications but with complete success only when cracks were aligned with element edges. The problem is associated with stress locking and has been understood for some time with solutions based on more complex numerical formulations. In order to retain the simplicity of the SCA, the solution proposed here was to modify the constitutive equation and remove the spurious stresses that arise because of the numerical procedure implicit with the conventional finite element method. By itself, this modification is not sufficient. The additional features of crack tracking and COS are necessary for accurately predicting the direction of crack propagation and the correct energy dissipation per unit length of crack. A nice additional advantage of the combination of spurious stress removal, crack following, and COS is that a specific continuous crack based on piecewise constant directions and widths is identified from the elements displaying cracks.

Positive results based on Mode-I failure and a limited number of examples only suggest that the proposed procedure justifies further investigation. Of the many topics, the following must be successfully addressed: failure of a single crack with a decohesive model that provides mixed-mode failure, crack branching, sharply curved cracks, and multiple cracks such as those often seen with blast loading.

The focus of an additional study to determine whether or not the procedure can be generalized would be to consider mixed-mode failure behavior through the use of a discrete constitutive model incorporating normal and tangential components of traction. Suppose that the corresponding mode of failure is described by the unit vector **m**. The analogous approach to that used in this paper would be to set any component of the displacement discontinuity perpendicular to **m** to zero. The result is that a linear combination of normal and shear components of the smeared-crack strain would be set to zero. On purpose, this paper considered a special case of this general approach to get the essential idea across in the simplest manner.

ORCID


D. J. Burnett https://orcid.org/0000-0003-3132-7463

REFERENCES

1. Rashid YR. Ultimate strength analysis of prestressed concrete pressure vessels. *Nucl Eng Des*. 1969;7(4):334-344.
2. Ngo D, Scordelis AC. Finite element analysis of reinforced concrete beams. *ACI J*. 1967;64(14):152-163.
3. Belytschko T, Black T. Elastic crack growth in finite elements with minimal remeshing. *Int J Numer Methods Eng*. 1999;45(5):601-620.
4. Miehe C, Welschinger F, Hofacker M. Thermodynamically consistent phase-field models of fracture: variational principles and multi-field FE implementations. *Int J Numer Methods Eng*. 2010;83(10):1273-1311.
5. Borden MJ, Verhoosel CV, Scott MA, Hughes TJR, Landis CM. A phase-field description of dynamic brittle fracture. *Comput Methods Appl Mech Eng*. 2012;217-220:77-95.
6. Bažant ZP, Lin F-B. Nonlocal smeared cracking model for concrete fracture. *J Struct Eng*. 1988;114(11):2493-2510.
7. Silling SA. Reformulation of elasticity theory for discontinuities and long-range forces. *J Mech Phys Solids*. 2000;48(1):175-209.
8. Hillerborg A, Modéer M, Petersson P-E. Analysis of crack formation and crack growth in concrete by means of fracture mechanics and finite elements. *Cem Concr Res*. 1976;6(6):773-781.
9. Bažant ZP. Instability, ductility, and size effect in strain-softening concrete. *ASCE J Eng Mech Div*. 1976;102(2):331-344.
10. Bažant ZP, Oh BH. Crack band theory for fracture of concrete. *Mater Struct*. 1983;16:155-177.
11. Kurumatani M, Terada K, Kato J, Kyoya T, Kashiyama K. An isotropic damage model based on fracture mechanics for concrete. *Eng Fract Mech*. 2016;155:49-66.
12. Rots JG. *Computational Modeling of Concrete Fracture* [PhD thesis]. Delft, The Netherlands: Delft University of Technology; 1988.
13. Rots JG. Smeared and discrete representations of localized failure. *Int J Fract*. 1991;51(1):45-59.
14. de Borst R, Nauta P. Non-orthogonal cracks in a smeared finite element model. *Eng Comput*. 1985;2(1):35-46.
15. Jirásek M, Zimmermann T. Analysis of rotating crack model. *J Eng Mech*. 1998;124(8):842-851.
16. Cervera M, Chiumenti M. Smeared crack approach: back to the original track. *Int J Numer Anal Methods Geomech*. 2006;30(12):1173-1199.
17. Cervera M. An orthotropic mesh corrected crack model. *Comput Methods Appl Mech Eng*. 2008;197(17-18):1603-1619.
18. Cervera M, Chiumenti M, Codina R. Mesh objective modeling of cracks using linear strain and displacement interpolations. *Int J Numer Methods Eng*. 2011;87(10):962-987.

19. Ortiz M, Leroy Y, Needleman A. A finite element method for localized failure analysis. *Comput Methods Appl Mech Eng*. 1987;61(2):189-214.
20. Belytschko T, Fish J, Engelmann BE. A finite element with embedded localization zones. *Comput Methods Appl Mech Eng*. 1988;70(1):59-89.
21. Dvorkin EN, Cuitiño AM, Gioia G. Finite elements with displacement interpolated embedded localization lines insensitive to mesh size and distortions. *Int J Numer Methods Eng*. 1990;30(3):541-564.
22. Linder C, Armero F. Finite elements with embedded strong discontinuities for the modeling of failure in solids. *Int J Numer Methods Eng*. 2007;72(12):1391-1433.
23. Jirásek M. A comparative study on finite elements with embedded discontinuities. *Comput Methods Appl Mech Eng*. 2000;188(1-3):307-330.
24. Hughes TJR. *The Finite Element Method: Linear Static and Dynamic Finite Element Analysis*. Mineola, NY: Dover Publication Inc; 2000.
25. Burnett DJ. *A Mesh Objective Algorithm for Modeling Mode-I Cracks Using a Standard Finite Element Formulation* [PhD thesis]. Albuquerque, NM: University of New Mexico; 2015.
26. Xu L, Schreyer H, Sulsky D. Blast-induced rock fracture near a tunnel. *Int J Numer Anal Methods Geomech*. 2014;39(1):23-50.
27. Oliver J. Modelling strong discontinuities in solid mechanics via strain softening constitutive equations. Part 1: fundamentals. *Int J Numer Methods Eng*. 1996;39(21):3575-3600.
28. Jirásek M, Zimmermann T. Rotating crack model with transition to scalar damage. *J Eng Mech*. 1998;124(3):277-284.
29. Geers MGD, de Borst R, Peerlings RHJ. Damage and crack modeling in single-edge and double-edge notched concrete beams. *Eng Fract Mech*. 2000;65(2-3):247-261.
30. Cervera M, Chiumenti M. Mesh objective tensile cracking via a local continuum damage model and a crack tracking technique. *Comput Methods Appl Mech Eng*. 2006;196(1-3):304-320.
31. Slobbe AT, Hendriks MAN, Rots JG. Smoothing the propagation of smeared cracks. *Eng Fract Mech*. 2014;132:147-168.
32. Saloustros S, Pelà L, Cervera M. A crack-tracking technique for localized cohesive-frictional damage. *Eng Fract Mech*. 2015;150:96-114.
33. Flanagan DP, Belytschko T. A uniform strain hexahedron and quadrilateral with orthogonal hourglass control. *Int J Numer Methods Eng*. 1981;17(5):679-706.
34. Nooru-Mohamed MB. *Mixed-Mode Fracture of Concrete: An Experimental Approach* [PhD thesis]. Delft, The Netherlands: Delft University of Technology; 1992.

How to cite this article: Burnett DJ, Schreyer HL. A mesh objective method for modeling crack propagation using the smeared crack approach. *Int J Numer Methods Eng*. 2018;1–30. https://doi.org/10.1002/nme.5968

APPENDIX A

CRACK TRACKING ALGORITHM DETAILS

The following crack tracking algorithm proposed is not necessarily the only way that it can be implemented within a code. There might be a more efficient computational way to construct the arrays and we leave it up to the reader to find other such possibilities. We begin by introducing a patch of nine quadrilateral finite elements where a crack initiates first in element B as shown in Figure A1. This crack starts an individual crack branch. The patch contains eight adjacent elements defined by the Southwest element (SW), South (S), and so on. Because the location of the crack is immaterial for obtaining the smeared crack strain, we choose the crack segment to go through the center of initiated element (element B in this instance). The coordinates of element B of the first initiated element are defined with (x_c, y_c) and the orientation of the initiated crack is defined with the crack normal vector $\mathbf{n_b}$. The intersection of the line segment representing the initiated crack with the element edges is denoted as the cracked element edge coordinates (CEECs). The CEECs of the first initiated crack are defined with (x_1^c, y_1^c) and (x_2^c, y_2^c). The local node numbering convention for all elements is shown for the center element in Figure A1. The starting crack coordinates (SCCs) are the coordinates of the crack root that start each crack segment after the first initiated crack and they are either (x_1^e, y_1^e) or (x_2^e, y_2^e). This convention helps generalize the CEECs equations into three categories as shown in Appendix B. For subsequent cracked elements traveling away from the first initiated crack, a similar approach is applied to define the crack normals and CEECs. For example, for a crack traveling northward, the CEECs that must be updated are denoted as (x_2^e, y_2^e), where e denotes corresponding CEECs of the adjacent element. For cracks traveling southward, the CEECs that must be updated are (x_1^e, y_1^e).

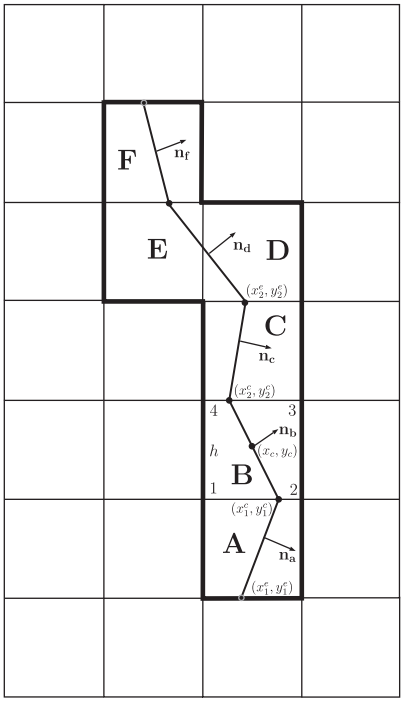

FIGURE A1 Tracking a crack through a mesh

For simplicity and consistency with a single crack forming in an element, one point integration is assumed. Here, the mesh is assumed regular defined by horizontal (x) and vertical (y) lines. With reference to Figure A1, the following algorithm is followed:

1. We identify element B as having a crack. Elements C (above) and A (below) are identified as specific elements to be tested for crack initiation to indicate when the crack propagates.
2. Suppose element C next indicates a crack initiation with normal $\mathbf{n}_c$ which, in general, is not the same as $\mathbf{n}_b$. We adjust the location of this crack segment so that it is continuous with the crack segment in element B. Now, element D (above C) is identified as an element to be followed for crack initiation.
3. Suppose element A is the next one to show crack initiation. A process similar to Step 2 is followed and the element below element A is identified as one to be checked for crack initiation with continued load steps.
4. Now, if element D is the next element to initiate a crack segment with normal $\mathbf{n}_d$, the crack segment is made continuous with that in element C. However, now the crack segment passes through portions of two elements: element D and element E. Elements D and E are called crossover elements and are forced to have identical characteristic crack lengths h_c, where $h_c = h^D + h^E$. The element dimensions for elements D and E are h^D and h^E, respectively. If no change is made to the characteristic crack length for crossover elements, the dissipated fracture energy is too large or the rate of unloading is to small. The adjustment to h_c causes the crossover elements to unload at about the same rate as a single element that is adjacent to the crossover (eg, element C).
5. Element F is now designated as the element to be followed for crack continuation.

Let us now introduce a computational array of integers E_{adj} of dimension $N_{ele} \times 8$ that contains the adjacent element numbers associated with each element in the mesh, where N_{ele} is the number of elements. For example, the eight adjacent element numbers associated with element number 10, would be stored in the 10th row of E_{adj} with adjacent element numbers stored along the columns as follows: SW, S, SE, E, NE, N, NW, W, and SW. This array is used to conveniently determine which elements are next in line to fail based on the CEECs of the current crack as discussed later. This array is formed during preprocessing.

Next, we introduce another computational array of integers C_{cond} of dimension $N_{ele} \times 3$. This array is used to apply flags that control which elements are allowed to fail and which require COS. The first column of C_{cond} stores a value of 1 in the e_n row for elements that have initiated a crack branch where e_n is the element number. Taking the sum of all elements in the first column of C_{cond} is equal to the total number of independent crack branches or separate initiated cracks. However,

to save computational expense, an accumulated sum of the total initiated number of cracks N_{cr} is determined and stored. Once the total number of allowed crack branches N_{crall} are formed, then the algorithm no longer allows new cracks to initiate. The second column of C_{cond} is used to store the crack condition number. The crack condition number is either 0, 1, or 2. A crack condition number of 0 (default) indicates the element has not yet cracked and is not slated for cracking in the next strain increment. A crack condition number of 1 indicates that the crack tracking algorithm has identified potential adjacent elements that intersect an evolving crack and these elements are now allowed to fail if the failure model deems it is appropriate. If the crack condition number is 2, then the crack is active and evolving. The third column of C_{cond} is used to store the crossover flag I_{cross}. If $I_{cross} = 0$ (default), then the current crack is not part of a crossover. However, if $I_{cross} = 1$, then the cracked element is within a crossover and h_c is adjusted such that it is equal to the sum of the characteristic element dimensions that are within the crossover.

Finally, an array of doubles C_{dbl} of dimension $N_{ele} \times 8$ is formed and the following components are stored in columns 1 through 8, respectively: N_1, N_2, T_1, T_2, x_1^e, y_1^e, x_2^e, and y_2^e, where N_1 is the $\mathbf{e}_1$ component of the crack normal vector $\mathbf{n}$, N_2 is the $\mathbf{e}_2$ component of the crack normal vector $\mathbf{n}$, T_1 is the $\mathbf{e}_1$ component of the crack tangential vector $\mathbf{t}$, T_2 is the $\mathbf{e}_2$ component of the crack tangential vector $\mathbf{t}$, and the CEECs are stored in (x_1^e, y_1^e) and (x_2^e, y_2^e).

Once failure initiation is detected, which is easily known once the decohesion function $F > 0$, the crack tracking algorithm must decide what failure scenario to engage from the following options: (1) the crack is newly initiated, (2) the crack is in an adjacent element, or (3) the crack is evolving. The framework of these choices is placed inside the failure model subroutine in the form of if-elseif statements. The first option or a newly initiated crack always occurs first because it is assumed that a propagating crack requires a single point of failure to start things off.

To identify scenario (1), the state of the crack condition array C_{cond} and the number of initiated cracks N_{cr} is examined. If $C_{cond}(e_n, 1) = 0$ and $N_{cr} < N_{crall}$, then the crack is newly initiated and the following actions are completed: (1a) increment the current number of initiated cracks N_{cr}, (1b) set $C_{cond}(e_n, 1) = 1$, (1c) set the CEECs compute flag $C_{\text{ceecs}} = 1$, (1d) set $C_{cond}(e_n, 2) = 2$, (1e) compute the CEECs, (1f) extract the adjacent elements that intersect current crack, (1g) set $C_{cond}(N_{adj}, 2) = 1$ where N_{adj} are the element numbers of the adjacent elements that are intersected by the initiated crack and are slated next for cracking, and (1h) update crack information array C_{dbl}. In step (1c), the CEECs compute flag C_{ceecs} is an integer between 1 and 3 that is used to identify which set of CEECs equations are to be used. The CEECs equations are derived and stated in Appendix A.

Failure scenario (2) is identified by checking the value of C_{cond}. If $C_{cond}(e_n, 2) = 1$, then the adjacent element that was flagged in scenario (1) has now cracked. As a result, the following actions are performed: (2a) set $C_{cond}(e_n, 2) = 2$, (2b) determine the CEECs compute flag and SCCs, (2c) compute the CEECs, (2d) extract the adjacent elements that intersect current crack, (2e) set $C_{cond}(N_{adj}, 2) = 1$, and (2f) update the crack information array C_{dbl}.

Finally, scenario (3) is identified by checking the value of C_{cond}. If $C_{cond}(e_n, 2) = 2$, then the crack is evolving and the stress in the element is updated according to Equations 38 through 40. No other actions are necessary. See Appendix A for more details.

APPENDIX B

DERIVATION OF CRACKED ELEMENT EDGE COORDINATES

The CEECs are used in the crack tracking algorithm to compute the path of the crack through the mesh based on the crack orientation $\mathbf{n}$ and the SCCs of the initiated crack denoted (x_{cr}^e, y_{cr}^e). The SSCs are the coordinates of the crack root that start each crack segment after the first initiated crack has formed and they are either (x_1^e, y_1^e) or (x_2^e, y_2^e) from the previous cracked element in the crack branch. For example, for cracked element 1 in Figure B1, the SCCs are $(x_{cr}^1, y_{cr}^1) = (x_2^n, y_2^n)$, where (x_2^n, y_2^n) are the CEECs for the North element (N). For tracking cracks in problems considered here, we define three sets of CEECs: (1) coordinates for first initiated cracks (x_1^c, y_1^c) and (x_2^c, y_2^c), (2) coordinates (x_2^e, y_2^e) for the crack segment leading off of either (x_2^c, y_2^c) or (x_{cr}^e, y_{cr}^e), and (3) coordinates (x_1^e, y_1^e) leading off of either (x_1^c, y_1^c) or (x_{cr}^e, y_{cr}^e). Note that, for case (1), the first initiated cracks are those that initiate a crack branch. As a result, (x_1^c, y_1^c) and (x_2^c, y_2^c) are computed only twice in the simulation.

The general procedure for deriving the CEECs is to express the equation of the line representing the crack segment in terms of the crack orientation $\mathbf{n}$ and another equation for the line representing the element edge that corresponds to the CEECs that are to be computed. These two equations are then solved simultaneously to determine the CEECs. The first equation is formed by taking the dot product of the normal vector $\mathbf{n}$ and a vector defining the crack segment in terms

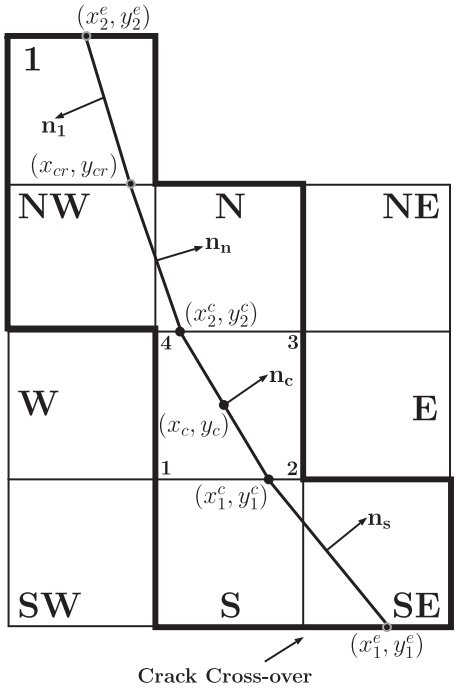

FIGURE B1 Tracking a crack through a mesh

of nodal coordinates. The second equation is formed by using the point-slope formula and setting $x = x_i^e$ and $y = y_i^e$. Applying this for case (1), we have

$$0 = \left(x_1^c - x_c\right) n_1 + \left(y_1^c - y_c\right) n_2 \tag{B1}$$

$$0 = \frac{x_1^c - x_1}{x_2 - x_1} - \frac{y_1^c - y_1}{y_2 - y_1}, \tag{B2}$$

where n_1 and n_2 are the vector components of $\mathbf{n}$ in the global $\{x, y\}$ coordinate system, (x_i, y_i) are the nodal coordinates, and (x_c, y_c) are the coordinates for the element center corresponding to the first initiated crack. Solving Equations B1 and B2 results in

$$x_1^c = \frac{[x_2\, y_1 - x_1\, y_2 + (x_1 - x_2) y_c]\, n_2 + (x_1 - x_2) n_1\, x_c}{(x_1 - x_2) n_1 + (y_1 - y_2) n_2} \tag{B3}$$

$$y_1^c = \frac{[x_1\, y_2 - y_1 x_2 + (y_1 - y_2) x_c]\, n_1 + (x_1 - x_2) n_2\, y_c}{(x_1 - x_2) n_1 + (y_1 - y_2) n_2} \tag{B4}$$

$$x_2^c = \frac{[x_4\, y_3 - x_3\, y_4 + (x_3 - x_4) y_c]\, n_2 + (x_3 - x_4) n_1\, x_c}{(x_3 - x_4) n_1 + (y_3 - y_4) n_2} \tag{B5}$$

$$y_2^c = \frac{[x_3\, y_4 - y_3 x_4 + (y_3 - y_4) x_c]\, n_1 + (y_3 - y_4) n_2\, y_c}{(x_3 - x_4) n_1 + (y_3 - y_4) n_2}. \tag{B6}$$

If we have a first initiated crack starting a crack branch, the CEECs compute flag is set to 1 and Equations B3 through B6 are used to compute the CEECs.

Following a similar procedure from the previous example and setting up equations for the crack segments leading from (x_2^c, y_2^c) and (x_1^c, y_1^c) result in the CEECs equations for cases (2) and (3), respectively, as follows:

$$x_2^e = \frac{[x_4\, y_3 - x_3\, y_4 + (x_3 - x_4) y_{cr}]\, n_2 + (x_3 - x_4) n_1\, x_{cr}}{(x_3 - x_4) n_1 + (y_3 - y_4) n_2} \tag{B7}$$

$$y_2^e = \frac{[x_3\, y_4 - y_3 x_4 + (y_3 - y_4) x_{cr}]\, n_1 + (y_3 - y_4) n_2\, y_{cr}}{(x_3 - x_4) n_1 + (y_3 - y_4) n_2} \tag{B8}$$

$$x_1^e = \frac{[x_2\, y_1 - x_1\, y_2 + (x_1 - x_2) y_{cr}]\, n_2 + (x_1 - x_2) n_1\, x_{cr}}{(x_1 - x_2) n_1 + (y_1 - y_2) n_2} \tag{B9}$$

$$y_1^e = \frac{[x_1\, y_2 - y_1 x_2 + (y_1 - y_2) x_{cr}]\, n_1 + (x_1 - x_2) n_2\, y_{cr}}{(x_1 - x_2) n_1 + (y_1 - y_2) n_2}. \tag{B10}$$

For case (2), we set the CEECs compute flag to 2 and Equations B7 and B8 are used to compute the CEECs. Finally, for case (3), the CEECs compute flag is set to 3 and Equations B9 and B10 are used to compute the CEECs.

All that is required to compute current crack segment information is the crack normal $\mathbf{n}$ of the current initiated crack, the SCCs, (x_{cr}^e, y_{cr}^e), which are equal to either (x_1^e, y_1^e) or (x_2^e, y_2^e) from the previous cracked element in the crack branch, and the nodal coordinates of the current initiated cracked element or the adjacent element that is slated to crack next. The CEECs and the adjacent element array E_{adj} are used to choose which elements are next in line to fail. If one of the adjacent elements has cracked, then a search is performed to find which element is evolving a crack or which element has a crack condition code $C_{cond}(n_e, 2) = 2$. The CEECs compute flag and SCCs are then chosen based on which position in the adjacent element array the evolving crack is located. Then, the next set of adjacent elements are determined using logic comparisons based on comparisons between the CEECs and the nodal coordinates of the evolving cracked element. This process continues as new cracks initiate.

For crack paths that involve an inflection in the crack path, then slight modifications to the SCCs and CEECs compute flag are necessary. For example, in the DEN direct-tension simulations, the crack normal component in the x-direction n_1 changes sign as the crack path goes downward for the top crack (or upward for the bottom crack). In the *Get-Crack* subroutine, which determines the SCCs and the CEECs compute flag, a search is performed to identify when a crack inflection occurs. If the condition is true, then the SCCs and compute flags for cases (2) and (3) are switched. The CEECs are then computed with the swapped SCCs and CEECs compute flag in the *Compute-CEECs* subroutine.